

# Enhanced H<sub>2</sub>O adsorption by Ca<sup>2+</sup> doping substantially improves the catalytic performance for light-driven thermocatalytic steam cellulose reforming on Ni/Ca<sub>1/8</sub>-SiO<sub>2</sub>

Jichun Wu, Yuanzhi Li\*, Chongyang Zhou, Qianqian Hu, Mengqi Zhong, Huamin Cao, Yaqi Hu, Lei Ji

*State Key Laboratory of Silicate Materials for Architectures (Wuhan University of Technology), 122 Luoshi Road, Wuhan 430070, PR China*



## ARTICLE INFO

### Keywords:

Light-driven thermocatalytic  
Steam cellulose reforming  
Hydrogen-rich syngas  
Ni catalyst  
Ca<sup>2+</sup> doping

## ABSTRACT

Using renewable biomass to produce syngas can form a closed carbon cycle, curbing carbon emissions. However, thermocatalysis suffers from high energy consumption, while the reaction rates of photocatalysis are relatively low. Here, we report the light-driven thermocatalytic steam cellulose reforming to hydrogen-rich syngas on the Ni nanoparticles loaded on Ca<sup>2+</sup> doping SiO<sub>2</sub> (Ni/Ca<sub>1/8</sub>-SiO<sub>2</sub>). It exhibits a high production rate of hydrogen-rich syngas (H<sub>2</sub> 3059.4 and CO 1612.1 mmol g<sup>-1</sup> catalyst h<sup>-1</sup>) and good cycling durability. Tar from cellulose pyrolysis, which is inherently challenging to prevent, is substantially decreased by the involvement of H<sub>2</sub>O. Ca<sup>2+</sup> doping dramatically enhances H<sub>2</sub>O adsorption, resulting in a significant improvement in catalytic performance. The efficient light-driven thermocatalysis derives from the strong absorption over the whole solar spectrum of Ni/Ca<sub>1/8</sub>-SiO<sub>2</sub> on the one hand. On the other hand, noticeable photoactivation effect is observed to promote the oxidation of carbon species by oxygen due to the surface Ni-O bonds being activated upon light illumination.

## 1. Introduction

Syngas (comprising of H<sub>2</sub> and CO) production plays a vital role in the chemical industry as it is a fundamental raw material for producing high value-added chemicals or fuels [1–5]. Traditionally, syngas is mainly produced by the thermocatalytic reforming of non-renewable fossil fuels such as coal, oil, and natural gas. This leads to a release of greenhouse gases, resulting in global warming and frequent extreme weather [6]. Biomass is a renewable and resource-rich energy source. Utilizing it as the feedstock for producing syngas will effectively help close carbon cycle and reduce carbon emissions.

To date, biomass conversion to value-added chemicals and fuels is mainly achieved by pyrolysis [7,8], thermocatalysis [9–16] and photocatalysis [17–33]. Both pyrolysis and thermocatalysis are typically performed at high temperatures to decompose biomass, leading to an increased energy consumption. Additionally, its high tar selectivity results in reduced syngas yield and may lead to reactor clogging and corrosion [9–16]. To cut down energy consumption, scientific researchers have focused on photocatalytic biomass conversion on semiconductor photocatalysts using renewable solar energy [17–33]. In

general, solar radiation excites the electrons in the valence bands of the semiconductor photocatalysts to the conduction bands, leaving holes in the valence bands. The electrons participate in the reduction of electron acceptors, while the holes participate in the oxidation of electron donors [34–36]. Due to the band gap matching requirement by photocatalysis, it is very difficult to efficiently utilize infrared light, which accounts for above 50 % of solar energy, resulting in a relatively low reaction rate [37].

Recently, by combining the advantages of photocatalysis (low energy consumption) and thermocatalysis (high production rate), light-driven thermocatalysis has been applied to CO<sub>2</sub> reduction [38–45], VOCs oxidation [46–48], hydrogenation [49–52], water-gas shift [53,54], and so on. Very recently our previous work [37] has demonstrated that it is an efficient route for producing hydrogen-rich syngas through light-driven thermocatalytic steam biomass reforming by using a catalyst of mesoporous silica supported Ni nanoparticles. It is important and of grand challenge to further significantly improve syngas production rate and reduce the amount of tar and char as by-products.

Biomass reforming involves the adsorption and dissociation of H<sub>2</sub>O to oxygen and hydrogen species, the pyrolysis of biomass to very

\* Corresponding author.

E-mail address: [liyuanzhi@whut.edu.cn](mailto:liyuanzhi@whut.edu.cn) (Y. Li).

complicated carbon-contained species, and the oxidation of the carbon-contained species by oxygen species [37]. It is expected that the enhanced H<sub>2</sub>O adsorption and dissociation is helpful to promote biomass steam reforming. In this work, we report a catalyst of Ni nanoparticles loaded on silica doped by Ca<sup>2+</sup> ions (denoted as Ni/Ca<sub>1/8</sub>-SiO<sub>2</sub>) for efficient light-driven thermocatalytic biomass cellulose reforming. We find that the Ca<sup>2+</sup> doping enhances the adsorption of H<sub>2</sub>O, leading to a considerable increase in hydrogen-rich syngas production and a substantial decrease in tar selectivity. We also find that focused illumination significantly enhances syngas production rate as compared to that in the dark (photoactivation). Based on a number of experimental evidences, we put insight in the role of Ca<sup>2+</sup> doping and the photoactivation.

## 2. Experimental

### 2.1. Preparation

The catalyst supports with varying amounts of Ca<sup>2+</sup> ions were prepared following the procedure. 11.3680 g of Na<sub>2</sub>SiO<sub>3</sub>·9 H<sub>2</sub>O were dissolved in 80 g deionized H<sub>2</sub>O in four separate beakers. Meanwhile, 0, 0.3675, 0.7351, and 1.4701 g (The molar ratio of Ca/Si are 0, 1/16, 1/8, and 1/4, respectively.) of CaCl<sub>2</sub>·2 H<sub>2</sub>O were dissolved in 40 g deionized H<sub>2</sub>O in another four different beakers. Afterward, the aqueous solution was added to the Na<sub>2</sub>SiO<sub>3</sub> solution dropwise with magnetic stirring. After being stirred for 1 h, a solution of C<sub>4</sub>H<sub>6</sub>O<sub>6</sub> with a concentration of 1 mol L<sup>-1</sup> was added to the mixed solution dropwise with magnetic stirring to adjust pH≈ 10. After being stirred for 0.5 h, we continued to adjust pH≈ 8 by slowly adding the C<sub>4</sub>H<sub>6</sub>O<sub>6</sub> solution with magnetic stirring. After stirring for another 1 h, the resulting suspension was sealed in the beakers with preservative film and aged in an electric oven at 90 °C for 24 h. After cooling to room temperature (RT), the precipitation was vacuum filtered, washed with deionized H<sub>2</sub>O, and dried at 180 °C for 12 h. Then the solid was evenly ground and calcined at 700 °C for 2 h in a muffle furnace with a heating rate of 10 °C min<sup>-1</sup> from RT to 700 °C. The obtained powders were denoted as SiO<sub>2</sub>, Ca<sub>1/16</sub>-SiO<sub>2</sub>, Ca<sub>1/8</sub>-SiO<sub>2</sub>, and Ca<sub>1/4</sub>-SiO<sub>2</sub>, respectively.

The catalysts of Ni nanoparticles loading on supports containing varying content of Ca<sup>2+</sup> were prepared according to the following procedure. 0.23 g Ni(CH<sub>3</sub>COO)<sub>2</sub>·4 H<sub>2</sub>O was added in four evaporating dishes, respectively. Then 5 mL diluted ammonia (volume ratio of concentrated ammonia (25–28 wt%) to H<sub>2</sub>O is 1:3) was added in the dishes, respectively, to dissolve the Ni(CH<sub>3</sub>COO)<sub>2</sub>·4 H<sub>2</sub>O. After that, 1.0307 g of SiO<sub>2</sub>, Ca<sub>1/16</sub>-SiO<sub>2</sub>, Ca<sub>1/8</sub>-SiO<sub>2</sub>, and Ca<sub>1/4</sub>-SiO<sub>2</sub> (The weight ratio of Ni/(Ni and support) is 0.05.) were added to the dishes, respectively. The evaporating dishes were transferred on heating plates holding at 150 °C, respectively, to dry the paste by constantly grinding. After that, the powders were dried at 150 °C for 12 h in an electric oven. The powder obtained were labeled as Ni(OH)<sub>2</sub>/SiO<sub>2</sub>, Ni(OH)<sub>2</sub>/Ca<sub>1/16</sub>-SiO<sub>2</sub>, Ni(OH)<sub>2</sub>/Ca<sub>1/8</sub>-SiO<sub>2</sub>, and Ni(OH)<sub>2</sub>/Ca<sub>1/4</sub>-SiO<sub>2</sub>, respectively. Finally, the obtained samples were reduced in a quartz tubular reactor at 700 °C for 2 h with a 15 mL min<sup>-1</sup> flow of pure H<sub>2</sub>. The obtained catalysts were denoted as Ni/SiO<sub>2</sub>, Ni/Ca<sub>1/16</sub>-SiO<sub>2</sub>, Ni/Ca<sub>1/8</sub>-SiO<sub>2</sub>, and Ni/Ca<sub>1/4</sub>-SiO<sub>2</sub>, respectively.

### 2.2. Characterization

The chemical compositions of Ni/SiO<sub>2</sub>, Ni/Ca<sub>1/16</sub>-SiO<sub>2</sub>, Ni/Ca<sub>1/8</sub>-SiO<sub>2</sub>, and Ni/Ca<sub>1/4</sub>-SiO<sub>2</sub> were analyzed on an X-ray fluorescence (XRF) spectrometer (Axios advanced). X-ray diffraction (XRD) patterns were obtained from a diffractometer (Empyrean) with Cu K $\alpha$  radiation. Transmission electron microscopy (TEM) images and EDS mappings were collected on a transmission electron microscope (FEI Talos F200X). Specific surface area and pore volume were measured on an absorption instrument (ASAP 2020) using N<sub>2</sub> absorption at -196 °C. The compositions of the agricultural wastes were analyzed on a CHNS elemental analyzer (Vario EL cube, Elementar) (Table S1). The amount of char

produced by the reaction and the total amount of organic compounds in the wastes were determined by calcining the residual solid after reaction and agricultural wastes in a muffle furnace. Diffuse reflectance absorption spectra were recorded on a spectrophotometer (Lambda 750S). Fourier transform infrared (FTIR) spectra were recorded on a Nicolet 6700 IR spectrometer.

### 2.3. Light-driven thermocatalytic and photocatalytic tests

Light-driven thermocatalytic steam cellulose reforming on the samples was evaluated in a homemade light-driven thermocatalysis reactor (Scheme S1) [37]. A known amount of cellulose was mixed well with the catalyst according to a weight ratio of 15:1 by grinding them in an agate mortar. Then the deionized H<sub>2</sub>O with a weight ratio of about 1.9 to cellulose was dropped into the mixture. After being mixed evenly, a known amount of the paste containing 0.05 g of cellulose was added to a corundum crucible supported by a piece of aluminum silicate insulation cotton. Details of the reaction procedure and the analysis of produced gases have been reported in our previous work (Scheme S2) [37]. The power values of the UV-vis-IR,  $\lambda > 420$  nm, and  $\lambda > 560$  nm vis-IR illumination focused into the reactor are 6849.8, 5856.4, and 5076.1 mW, respectively. The diameter of the irradiated range of the mixture is 7 mm (the diameter of crucible). Their corresponding light intensity values are 178.0, 152.2, and 131.9 kW m<sup>-2</sup>, respectively.

The catalyst durability was tested according to the procedure as follows: After the light-driven thermocatalytic test mentioned above, a residual solid mixture of the catalyst and char, remained in an alumina crucible in the reactor, was collected. The amount of char in the solid mixture was measured by calcining the residual solid in a muffle furnace. Thus, the amount of catalyst in the residual solid was calculated. Then, cellulose was mixed with the residual solid according to a weight ratio of cellulose/catalyst of 15:1. Deionized H<sub>2</sub>O with a weight ratio of 1.9 to cellulose was dropped into the mixture. After the mixture was uniformly ground in an agate mortar, a known amount of the resultant mixture paste containing 0.05 g of cellulose was added in the reactor. The other procedure was the same as the above light-driven thermocatalytic test. As the mixture grinding procedure led to a loss of the mixture paste, more mixture paste was needed to be prepared for the next recycling test by using more the residual solid. Therefore, each light-driven thermocatalytic test was repeated for several times in parallel, thus more residual solid was collected for the next recycling test.

For dry cellulose pyrolysis under focused illumination, 0.05 g of the dry cellulose and catalyst with a weight ratio of 15:1 was compressed into a tablet.

For steam biomass reforming under focused illumination, the cellulose was replaced by the powder of rice straw, wheat straw, or corn stalk (Table S1). We tabulated the specific amounts of reactants for steam cellulose/biomass reforming (Table S2).

The photocatalytic reaction on Ni/Ca<sub>1/8</sub>-SiO<sub>2</sub> was conducted by placing the mixture on the reactor bottom kept at near room temperature (RT) in an ice-water bath.

### 2.4. Controlled catalytic tests

Controlled catalytic tests in a fixed bed with illumination or in the dark at varying temperatures were evaluated on a set-up, as reported in our previous work (Scheme S3) [37]. The reactor was heated at a rate of 5 °C min<sup>-1</sup> to 700 °C with focused illumination or in the dark.

For controlled catalytic steam cellulose reforming, the mixture was prepared by the same procedure for the light-driven thermocatalytic steam cellulose reforming described above. Then a known amount of the mixture containing 0.05 g cellulose was added in a tubular quartz reactor (Scheme S3). Before the reaction, we purged the system by high-purity Ar.

For controlled catalytic dry cellulose pyrolysis, the mixture was prepared by the same procedure for the light-driven thermocatalytic dry

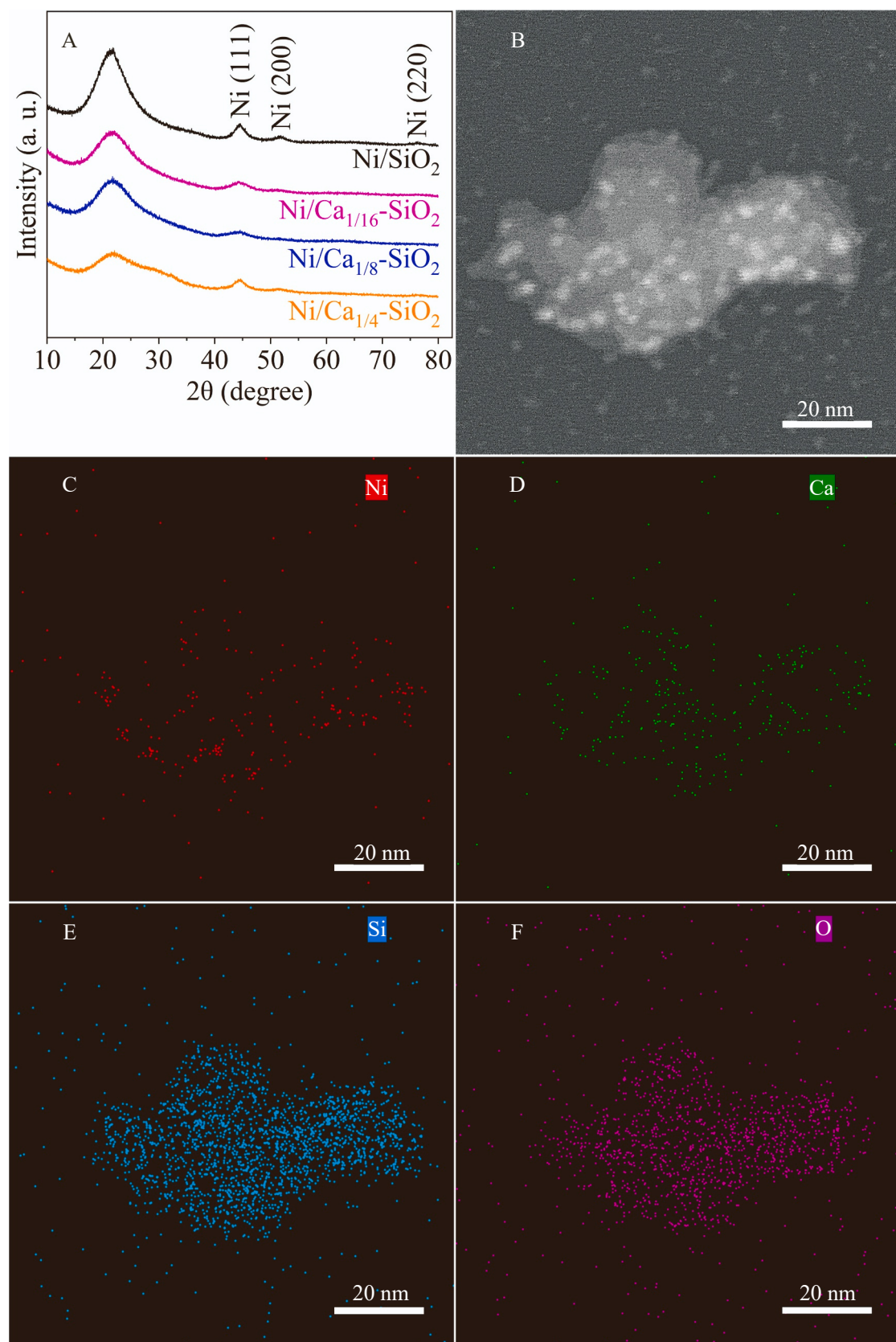


**Fig. 1.** XRD patterns of Ni/SiO<sub>2</sub>, Ni/Ca<sub>1/16</sub>-SiO<sub>2</sub>, Ni/Ca<sub>1/8</sub>-SiO<sub>2</sub>, and Ni/Ca<sub>1/4</sub>-SiO<sub>2</sub> (A), HAADF image (B), and corresponding EDS mappings of Ni (C), Ca (D), Si (E), and O (F) of Ni/Ca<sub>1/8</sub>-SiO<sub>2</sub>.

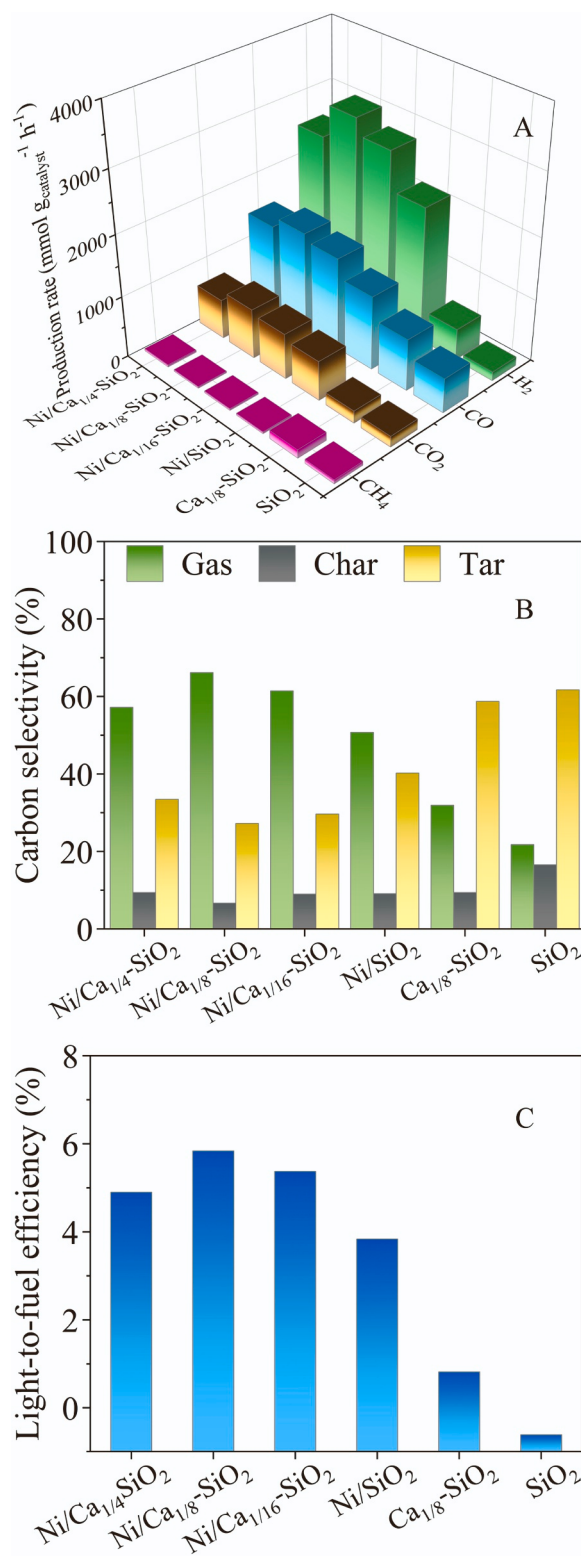


**Fig. 2.** Production rates (A), carbon selectivities of gas, char, and tar (B), and light-to-fuel efficiencies (C) of steam cellulose reforming on the catalysts under focused UV-vis-IR illumination.

cellulose pyrolysis described above without compressing them to be tablets. Before starting the reaction, the mixture was dried at 100 °C for 1 h in a 30 mL min<sup>-1</sup> high-purity Ar flow in the tubular quartz reactor.

For controlled catalytic pre-formed char reacting with adsorbed H<sub>2</sub>O, 0.64 g of the same mixture prepared for controlled catalytic dry cellulose

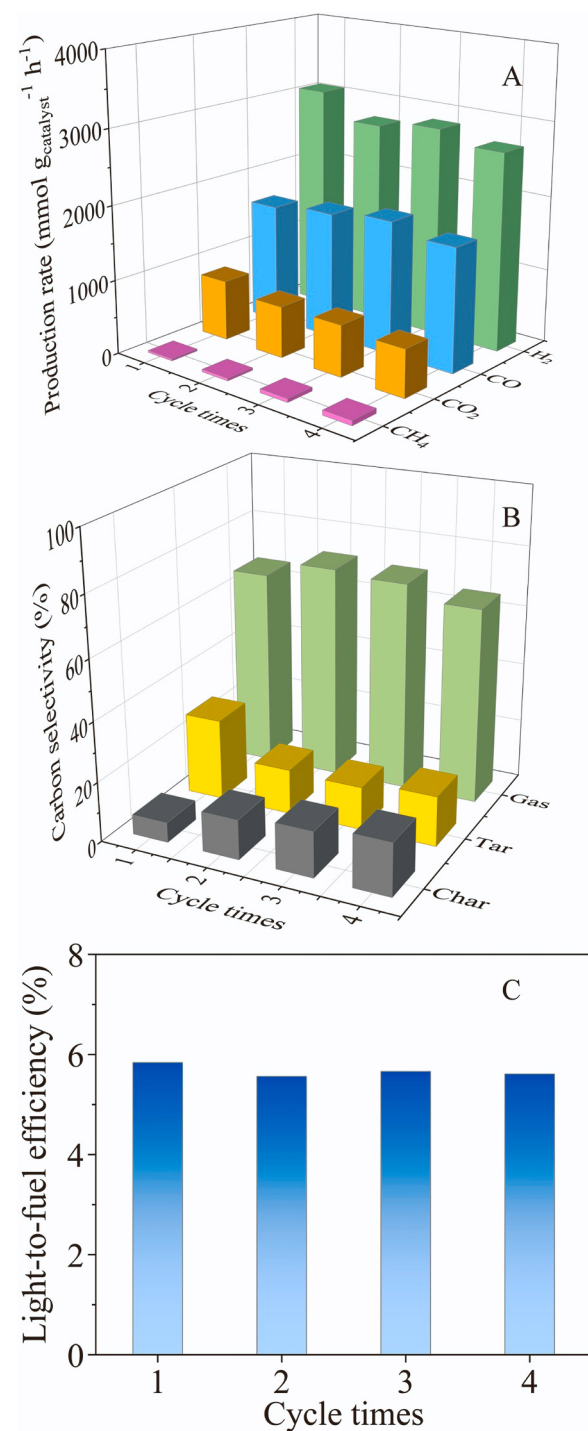


**Fig. 3.** Production rates (A), carbon selectivities of gas, char, and tar (B), and light-to-fuel efficiencies (C) of cycling steam cellulose reforming on Ni/Ca<sub>1/8</sub>-SiO<sub>2</sub> four times under focused UV-vis-IR illumination.

pyrolysis was placed in the tubular quartz reactor ([Scheme S4](#)). After a flow of high-purity Ar purged the system, the reactor was heated to 700 °C and held for 30 min. After cooling to RT, the residual solid containing about 0.01 g of char was placed in the tubular quartz reactor. High-purity Ar purged the system for 30 min with a flow rate of 30 mL min<sup>-1</sup>. Then the high-purity Ar was switched to pass through the bubbler containing deionized H<sub>2</sub>O before entering the reactor. After adsorbing H<sub>2</sub>O for 2 h, the system was purged by dry high-purity Ar flow for another 2 h.

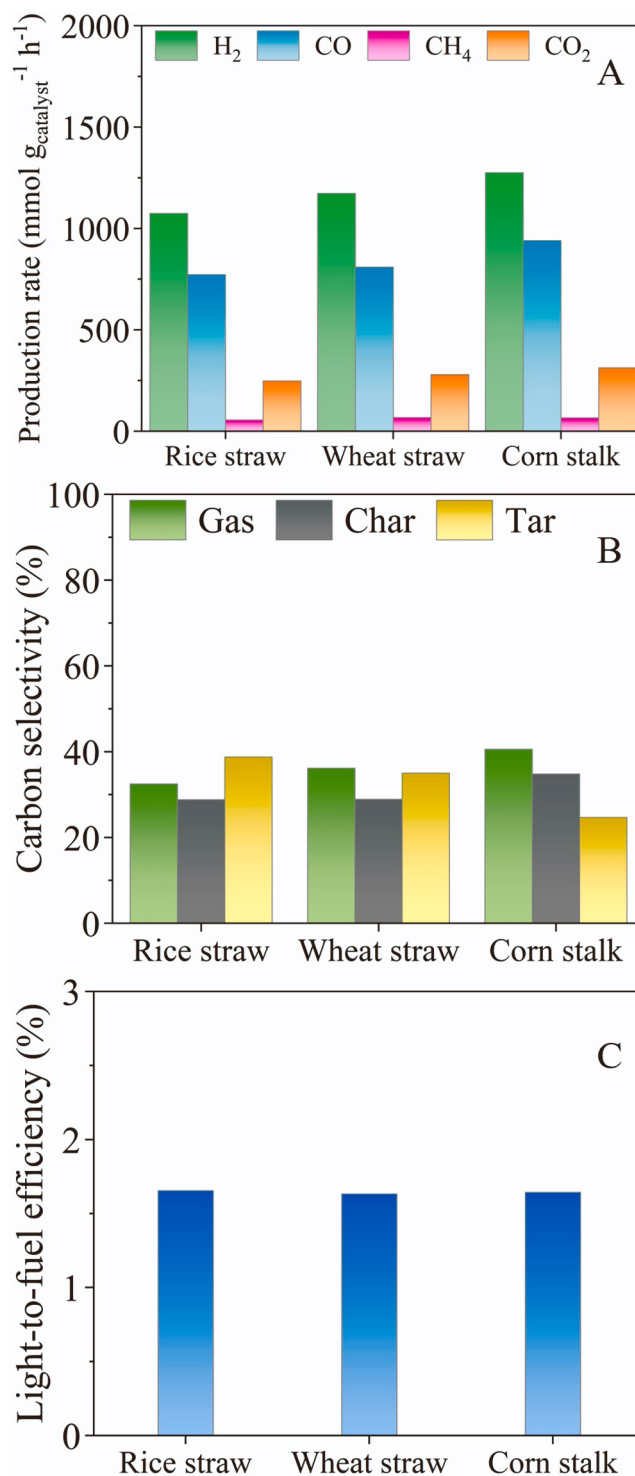


**Fig. 4.** Production rates (A), carbon selectivities of gas, char, and tar (B), and light-to-fuel efficiencies (C) of light-driven thermocatalytic steam rice straw, wheat straw, and corn stalk reforming on Ni/Ca<sub>1/8</sub>-SiO<sub>2</sub> under focused UV-vis-IR illumination.

## 2.5. Isotope labeling

Isotope labeling experiment of reaction between cellulose and H<sub>2</sub><sup>18</sup>O or adsorbed H<sub>2</sub><sup>18</sup>O on Ni/Ca<sub>1/8</sub>-SiO<sub>2</sub> or Ni/SiO<sub>2</sub> was performed in the homemade light-driven thermocatalysis reactor (**Scheme S1**) [37] too. The produced CO<sub>2</sub> and CO were analyzed by FTIR. For the reaction of cellulose and H<sub>2</sub><sup>18</sup>O, the procedure was the same as steam cellulose

reforming under focused illumination described above. For the reaction of cellulose and adsorbed H<sub>2</sub><sup>18</sup>O, 0.045 g of Ni/Ca<sub>1/8</sub>-SiO<sub>2</sub> or Ni/SiO<sub>2</sub> was impregnated in 0.045 g of H<sub>2</sub><sup>18</sup>O for 12 h. Then the catalyst was dried at 70 °C for 12 h. After that, 0.015 g of the catalyst was reduced in 5 vol% H<sub>2</sub>/Ar with a flow rate of 24 mL min<sup>-1</sup> at 200 or 400 °C for 0.5 h. Then the catalyst was mixed with dry cellulose according to a weight ratio of 1:2 by grinding them in an agate mortar. Finally, 0.045 g of the mixture was compressed to be a tablet. The other procedure was the same as light-driven thermocatalytic dry cellulose pyrolysis under focused illumination described above.

## 2.6. H<sub>2</sub>-TPR of pre-chemisorbed oxygen

H<sub>2</sub> temperature-programmed reduction (H<sub>2</sub>-TPR) of the pre-chemisorbed oxygen on the surface of Ni nanoparticles with paralleled illumination or in the dark was conducted on a TP5080 multifunctional adsorption apparatus using a tubular quartz reactor linked to a quartz window. 0.0050 g of Ni/Ca<sub>1/8</sub>-SiO<sub>2</sub> was fed into the reactor. The sample was heated to 700 °C at a rate of 10 °C min<sup>-1</sup> with a 24 mL min<sup>-1</sup> pure H<sub>2</sub> flow and held at 700 °C for 2 h. After cooling to RT, the gas was switched to 5 vol% O<sub>2</sub>/He with a flow rate of 24 mL min<sup>-1</sup> and kept at RT for 30 min. After that, the gas was switched to 5 vol% H<sub>2</sub>/Ar with a flow rate of 24 mL min<sup>-1</sup>. Finally, the sample was heated from RT to 700 °C with a heating rate of 10 °C min<sup>-1</sup> in 5 vol% H<sub>2</sub>/Ar flow with paralleled UV-vis-IR illumination or in the dark.

## 3. Results and discussion

### 3.1. Characterization

XRF analysis shows that the weight ratios of Ni in Ni/SiO<sub>2</sub>, Ni/Ca<sub>1/16</sub>-SiO<sub>2</sub>, Ni/Ca<sub>1/8</sub>-SiO<sub>2</sub>, and Ni/Ca<sub>1/4</sub>-SiO<sub>2</sub> are 5.22, 5.17, 4.88 and 5.14 wt%, respectively. Additionally, the molar ratio of Ca/Si in Ni/SiO<sub>2</sub>, Ni/Ca<sub>1/16</sub>-SiO<sub>2</sub>, Ni/Ca<sub>1/8</sub>-SiO<sub>2</sub>, and Ni/Ca<sub>1/4</sub>-SiO<sub>2</sub> are 0, 4.34, 9.83, and 21.99 mol%, respectively (**Table S3**). The XRD patterns of Ni/SiO<sub>2</sub>, Ni/Ca<sub>1/16</sub>-SiO<sub>2</sub>, Ni/Ca<sub>1/8</sub>-SiO<sub>2</sub>, and Ni/Ca<sub>1/4</sub>-SiO<sub>2</sub> (**Fig. 1A**) reveal that Ni species are present in a metallic nickel phase with a cubic structure (JCPDS No. 65–2865). Silica, on the other hand, are amorphous phase, which is identifiable by the broad peak ranging from 15° to 30°. By applying the Scherrer formula ( $L = 0.89\lambda/(\beta\cos\theta)$ ) to the peak corresponding to (111) facets ( $2\theta = 44.5^\circ$ ), average Ni crystal sizes are 4.4, 3.4, 3.5, and 4.2 nm in Ni/SiO<sub>2</sub>, Ni/Ca<sub>1/16</sub>-SiO<sub>2</sub>, Ni/Ca<sub>1/8</sub>-SiO<sub>2</sub>, and Ni/Ca<sub>1/4</sub>-SiO<sub>2</sub>, respectively (**Table S3**). No XRD peaks of Ca compounds are observed in Ni/Ca<sub>1/16</sub>-SiO<sub>2</sub>, Ni/Ca<sub>1/8</sub>-SiO<sub>2</sub>, and Ni/Ca<sub>1/4</sub>-SiO<sub>2</sub>, suggesting that Ca<sup>2+</sup> ions are highly dispersed. We mainly characterized the Ni/Ca<sub>1/8</sub>-SiO<sub>2</sub> due to its superior performance for light-driven thermocatalytic cellulose reforming (See **Section 3.2**). The HAADF image of Ni/Ca<sub>1/8</sub>-SiO<sub>2</sub> indicates well-distributed Ni nanoparticles (bright dots) on Ca<sub>1/8</sub>-SiO<sub>2</sub> (**Fig. 1B**). It also can be confirmed by EDS mapping of Ni (**Fig. 1C**) and TEM image of Ni/Ca<sub>1/8</sub>-SiO<sub>2</sub> (**Fig. S1A**, the black dots). In comparison, corresponding EDS mappings of Ca, Si, and O demonstrate that they are all uniformly distributed in Ni/Ca<sub>1/8</sub>-SiO<sub>2</sub> (**Fig. 1D–F**). HRTEM shows a distinct lattice spacing of 0.203 nm corresponding to (111) facets of Ni nanocrystals (**Fig. S1B**). No lattice spacing of Ca compounds or SiO<sub>2</sub> are observed in the HRTEM image of Ni/Ca<sub>1/8</sub>-SiO<sub>2</sub>.

The surface area and pore volume of the samples were measured by N<sub>2</sub> adsorption. The BET surface areas of Ni/SiO<sub>2</sub>, Ni/Ca<sub>1/16</sub>-SiO<sub>2</sub>, Ni/Ca<sub>1/8</sub>-SiO<sub>2</sub>, and Ni/Ca<sub>1/4</sub>-SiO<sub>2</sub> are 55.45, 168.94, 89.73, and 65.04 m<sup>2</sup> g<sup>-1</sup>, respectively (**Table S3**). The result indicates that a small amount of Ca<sup>2+</sup> doping (Ni/Ca<sub>1/16</sub>-SiO<sub>2</sub>) leads to a considerable increase in BET surface area, but further increasing Ca<sup>2+</sup> doping amount (Ni/Ca<sub>1/8</sub>-SiO<sub>2</sub> and Ni/Ca<sub>1/4</sub>-SiO<sub>2</sub>) results in a gradual reduction in BET surface area. The BJH adsorption volumes of Ni/SiO<sub>2</sub>, Ni/Ca<sub>1/16</sub>-SiO<sub>2</sub>, Ni/Ca<sub>1/8</sub>-SiO<sub>2</sub>, and Ni/Ca<sub>1/4</sub>-SiO<sub>2</sub> are 0.49, 0.72, 0.46, and 0.32 cm<sup>3</sup> g<sup>-1</sup>, respectively. Their average pore sizes are 35.9, 17.0, 20.6, and 19.8, respectively (**Table S3**, **Fig. S2, S3, S4 and S5**).

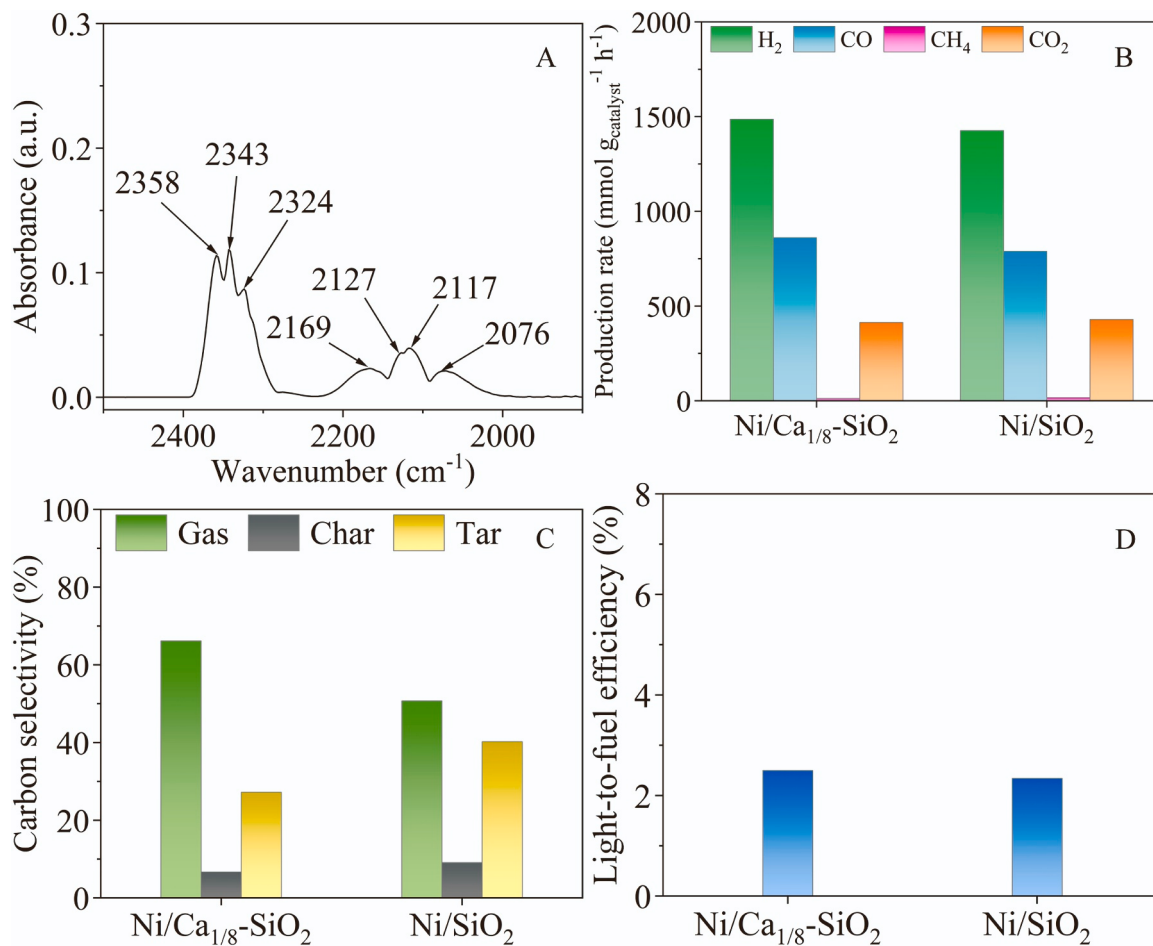


**Fig. 5.** FTIR spectra of CO and  $\text{CO}_2$  produced by cellulose reforming with  $\text{H}_2^{18}\text{O}$  on  $\text{Ni}/\text{Ca}_{1/8}\text{-SiO}_2$  for 9 min under focused UV-vis-IR illumination (A). Production rates (B), carbon selectivities of gas, char, and tar (C), and light-to-fuel efficiencies (D) of dry cellulose pyrolysis on  $\text{Ni}/\text{Ca}_{1/8}\text{-SiO}_2$  and  $\text{Ni}/\text{SiO}_2$  for 9 min under focused UV-vis-IR illumination.

### 3.2. Light-driven thermocatalytic performance

As shown in Fig. 2,  $\text{Ni}/\text{SiO}_2$  demonstrates good catalytic activity for cellulose steam reforming under focused UV-vis-IR illumination. After 9 min of illumination, its production rates of  $\text{H}_2$ ,  $\text{CO}$ ,  $\text{CH}_4$ , and  $\text{CO}_2$  are 2180.6, 1202.3, 30.7, and 644.9  $\text{mmol g}_{\text{catalyst}}^{-1} \text{h}^{-1}$ , respectively (Fig. 2A). Its selectivities of carbon for gas, char, and tar are 50.7 %, 9.1 % and 40.2 %, respectively (Fig. 2B). The molar ratio of  $\text{H}_2/\text{CO}$  ( $\approx 1.8$ ) is higher than the stoichiometric ratio (1.0) of steam cellulose reforming ( $(\text{C}_6\text{H}_{10}\text{O}_5)_n + n\text{H}_2\text{O} = 6n\text{CO} + 6n\text{H}_2$ ). It is mainly attributed to the side reaction of the Water-Gas Shift Reaction (WGSR:  $\text{H}_2\text{O} + \text{CO} = \text{H}_2 + \text{CO}_2$ ) [37]. Interestingly, a small amount of  $\text{Ca}^{2+}$  doping in  $\text{SiO}_2$  ( $\text{Ni}/\text{Ca}_{1/16}\text{-SiO}_2$ ) leads to a significant increase in the  $\text{H}_2$  and  $\text{CO}$  production rates, and a considerable decrease in the tar selectivity. By increasing the  $\text{Ca}^{2+}$ -doping amount, a catalyst of  $\text{Ni}/\text{Ca}_{1/8}\text{-SiO}_2$  with the best catalytic performance is obtained. Its production rates of  $\text{H}_2$ ,  $\text{CO}$ ,  $\text{CH}_4$ , and  $\text{CO}_2$  are 3059.4, 1612.1, 26.7, and 811.0  $\text{mmol g}_{\text{catalyst}}^{-1} \text{h}^{-1}$ , respectively. Its selectivities of carbon for gas, char, and tar are 66.1 %, 6.7 %, and 27.2 %, respectively (Fig. 2B). Further increasing the  $\text{Ca}^{2+}$  doping amount ( $\text{Ni}/\text{Ca}_{1/4}\text{-SiO}_2$ ) results in a slight reduction in activity probably due to a decrease in BET surface area and an increase in the size of Ni nanoparticles (Table S3). To reveal the catalytic active sites in  $\text{Ni}/\text{Ca}_{1/8}\text{-SiO}_2$ , we measured the catalytic activity of  $\text{Ca}_{1/8}\text{-SiO}_2$  as support in the same conditions. As shown in Fig. 2,  $\text{Ca}_{1/8}\text{-SiO}_2$  performs a low catalytic activity. Its production rates of  $\text{H}_2$ ,  $\text{CO}$ ,  $\text{CH}_4$ , and  $\text{CO}_2$  are 511.5, 842.6, 137.96, and 201.19  $\text{mmol g}_{\text{catalyst}}^{-1} \text{h}^{-1}$ , respectively. The selectivities of carbon for gas, char, and tar are 31.9 %, 9.4 %, and 58.7

%, respectively (Fig. 2B). The results show that Ni nanoparticles are the primary catalytic sites. To compare with  $\text{Ca}_{1/8}\text{-SiO}_2$ , the catalytic activity of  $\text{SiO}_2$  was also measured. The production rates of  $\text{H}_2$ ,  $\text{CO}$ ,  $\text{CH}_4$ , and  $\text{CO}_2$  are 144.7, 562.5, 66.1, and 177.2  $\text{mmol g}_{\text{catalyst}}^{-1} \text{h}^{-1}$ , respectively (Fig. 2A). The selectivities of carbon for gas, char, and tar are 21.8 %, 16.5 % and 61.7 %, respectively (Fig. 2B). This shows that  $\text{Ca}^{2+}$  doping slightly promotes the performance of  $\text{SiO}_2$  as support.

As a highly endothermic reaction ( $\Delta H_{298} = 1144.8 \text{ kJ mol}^{-1}$ ), the light-to-fuel efficiency ( $\eta$ ) of steam cellulose reforming is calculated by the following formula [37].

$$\eta = (r_{\text{CO}} \times \Delta_c H_{\text{CO}}^0 + r_{\text{H}_2} \times \Delta_c H_{\text{H}_2}^0 + r_{\text{CH}_4} \times \Delta_c H_{\text{CH}_4}^0 - r_{\text{C}_6\text{H}_{10}\text{O}_5, \text{gas}} \times \Delta_c H_{\text{C}_6\text{H}_{10}\text{O}_5}^0) \times m_{\text{catalyst}} / (P \times 3600)$$

$\Delta_c H_{\text{CO}}^0$ ,  $\Delta_c H_{\text{H}_2}^0$ ,  $\Delta_c H_{\text{CH}_4}^0$ , and  $\Delta_c H_{\text{C}_6\text{H}_{10}\text{O}_5}^0$  are the standard combustion heats (298.15 K) of CO,  $\text{H}_2$ ,  $\text{CH}_4$ , and cellulose as fuels, respectively.  $r_{\text{CO}}$ ,  $r_{\text{H}_2}$ , and  $r_{\text{CH}_4}$  represent production rates of CO,  $\text{H}_2$ , and  $\text{CH}_4$ , respectively.  $r_{\text{C}_6\text{H}_{10}\text{O}_5}$  is the reaction rate of cellulose consumed to produce gases.  $P$  (mW) represents illumination power [37].

The  $\eta$  values of  $\text{Ni}/\text{Ca}_{1/8}\text{-SiO}_2$ ,  $\text{Ni}/\text{SiO}_2$ , and  $\text{Ca}_{1/8}\text{-SiO}_2$  are 5.8 %, 3.8 %, and 0.8 %, respectively (Fig. 2C). As compared with light-driven biomass reforming that have been reported,  $\text{Ni}/\text{Ca}_{1/8}\text{-SiO}_2$  has exhibited excellent performance in the light-driven steam biomass reforming (Table S4).

We also evaluated the activity of  $\text{Ni}/\text{Ca}_{1/8}\text{-SiO}_2$  under focused  $\lambda > 420$  or  $\lambda > 560 \text{ nm}$  vis-IR illumination. Under focused  $\lambda > 420 \text{ nm}$  vis-IR illumination, the production rates of  $\text{H}_2$ ,  $\text{CO}$ ,  $\text{CH}_4$ , and  $\text{CO}_2$  are 2706.6, 1412.8, 26.3, and 766.1  $\text{mmol g}_{\text{catalyst}}^{-1} \text{h}^{-1}$ , respectively

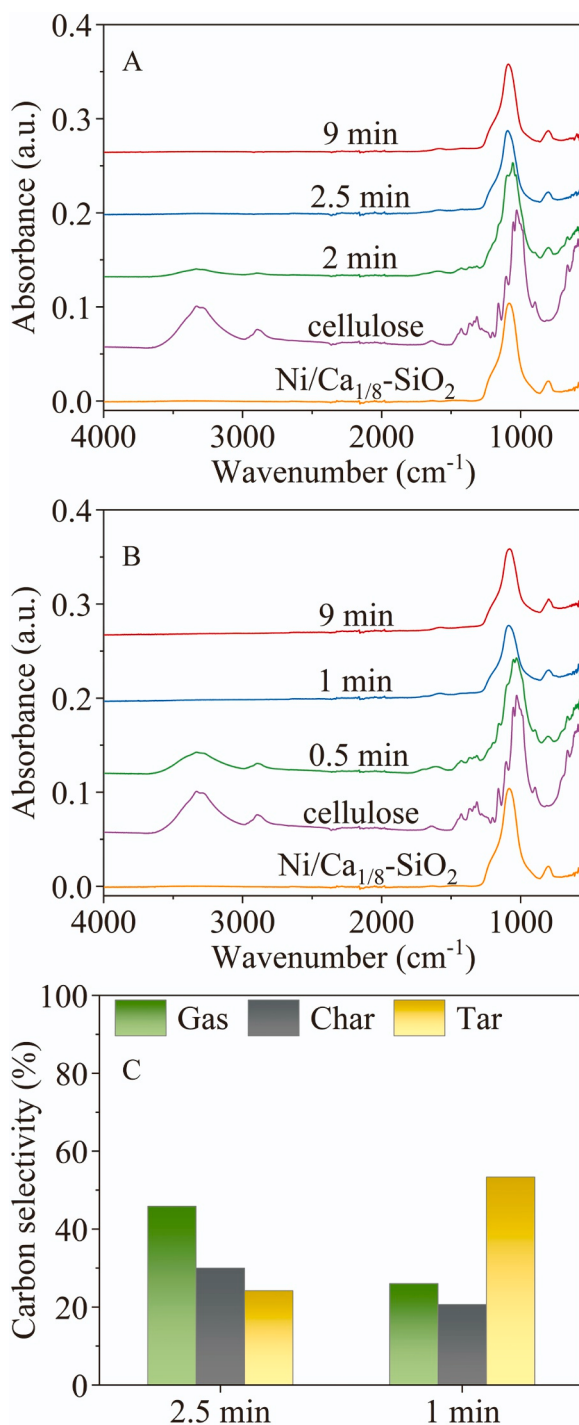


**Fig. 6.** FTIR spectra of fresh Ni/Ca<sub>1/8</sub>-SiO<sub>2</sub>, cellulose, and the residual solid after steam cellulose reforming (A) and dry cellulose pyrolysis (B) on Ni/Ca<sub>1/8</sub>-SiO<sub>2</sub> for specific times under focused UV-vis-IR illumination. Carbon selectivities of gas, char, and tar after steam cellulose reforming for 2.5 min and dry cellulose pyrolysis for 1 min on Ni/Ca<sub>1/8</sub>-SiO<sub>2</sub> (C).

(Fig. S6A). The carbon selectivities of gas, char, and tar are 29.5 %, 9.4 % and 31.1 %, respectively (Fig. S6B). Under focused  $\lambda > 560$  nm vis-IR illumination, H<sub>2</sub>, CO, CH<sub>4</sub>, and CO<sub>2</sub> production rates are 2390.3, 1175.8, 20.7, and 737.1 mmol g<sub>catalyst</sub><sup>-1</sup> h<sup>-1</sup>, respectively (Fig. S6A). The selectivities of carbon for gas, char, and tar are 52.2 %, 10.7 %, and 37.1 %, respectively (Fig. S6B). The  $\eta$  values of under focused  $\lambda > 420$ , and  $\lambda > 560$  nm vis-IR illumination are 5.8 %, and 5.6 %, respectively (Fig. S6C). Even the illumination intensity reduces from 178.0 kW m<sup>-2</sup>

(UV-vis-IR) to 131.9 kW m<sup>-2</sup> ( $\lambda > 560$  nm vis-IR), Ni/Ca<sub>1/8</sub>-SiO<sub>2</sub> still exhibited good performance in light-driven steam cellulose reforming.

Catalyst durability is crucial for practical applications, so we evaluated the light-driven thermocatalytic durability of Ni/Ca<sub>1/8</sub>-SiO<sub>2</sub> for steam cellulose reforming. After four cycles, the production rates of H<sub>2</sub> and CO are 2677.2 and 1668.1 mmol g<sub>catalyst</sub><sup>-1</sup> h<sup>-1</sup> (Fig. 3A). The selectivities of carbon for gas, char, and tar are 65.6 %, 17.6 % and 16.8 %, respectively (Fig. 3B). The  $\eta$  is 5.61 % (Fig. 3C). These results indicate that Ni/Ca<sub>1/8</sub>-SiO<sub>2</sub> exhibits good durability during steam cellulose reforming. To reveal the excellent durability of Ni/Ca<sub>1/8</sub>-SiO<sub>2</sub>, the residual solids were analyzed by Raman and TEM. As shown in Fig. S7A, Ni nanoparticles (black dots) still distribute well in Ni/Ca<sub>1/8</sub>-SiO<sub>2</sub> after the durability test. No visible sintering is observed compared to the fresh Ni/Ca<sub>1/8</sub>-SiO<sub>2</sub> (Fig. S1A). Despite the marked graphite-like char deposition on Ni/Ca<sub>1/8</sub>-SiO<sub>2</sub> after the durability test (Fig. S7C), the Ni nanoparticles still exhibit a clear lattice spacing in the (111) plane, illustrated in the HRTEM image (Fig. S7B). This suggests that the surface of Ni nanoparticle has not been entirely covered by the deposited char, which could hinder the contact between Ni nanoparticles and reactants, leading rapid deactivation. Consequently, Ni/Ca<sub>1/8</sub>-SiO<sub>2</sub> demonstrates reliable catalytic durability in the reaction.

As a comparison, we also tested the durability of Ni/SiO<sub>2</sub> under the same conditions as those of Ni/Ca<sub>1/8</sub>-SiO<sub>2</sub>. Ni/SiO<sub>2</sub> also shows good durability in the recycling tests (Fig. S8). However, the syngas production rates of Ni/SiO<sub>2</sub> are significantly lower than that of Ni/Ca<sub>1/8</sub>-SiO<sub>2</sub>, and the tar and char selectivities are significantly higher than those of Ni/Ca<sub>1/8</sub>-SiO<sub>2</sub>, which further demonstrates that Ca<sup>2+</sup> doping effectively promotes the catalytic activity and reduces the tar and char selectivities. The good durability of both Ni/Ca<sub>1/8</sub>-SiO<sub>2</sub> and Ni/SiO<sub>2</sub> indicates that Ni nanoparticles as main catalytic active components are stabilized by their supports of Ca<sub>1/8</sub>-SiO<sub>2</sub> and SiO<sub>2</sub> (Table S3) via their interaction (e.g. -Si-O-Ni- bonds), thus avoiding the sintering of Ni nanoparticles at high temperature under focused illumination.

In order to examine the performance of Ni/Ca<sub>1/8</sub>-SiO<sub>2</sub> in practical applications, we selected three primary agricultural wastes for steam biomass reforming under focused UV-vis-IR illumination. For rice straw, the production rates of H<sub>2</sub>, CO, CH<sub>4</sub>, and CO<sub>2</sub> are 1074.6, 772.5, 56.5, and 248.8 mmol g<sub>catalyst</sub><sup>-1</sup> h<sup>-1</sup>, respectively (Fig. 4A). The carbon selectivities of gas, char, and tar are 32.5 %, 28.8 %, and 38.7 %, respectively (Fig. 4B). H<sub>2</sub>, CO, CH<sub>4</sub>, and CO<sub>2</sub> production rates of wheat straw are 1173.2, 810.2, 68.2, and 279.9 mmol g<sub>catalyst</sub><sup>-1</sup> h<sup>-1</sup>, respectively (Fig. 4A). The carbon selectivities of gas, char, and tar are 36.1 %, 28.9 % and 35.0 %, respectively (Fig. 4B). For corn stalk, H<sub>2</sub>, CO, CH<sub>4</sub>, and CO<sub>2</sub> production rates are 1275.5, 940.6, 66.5, and 313.3 mmol g<sub>catalyst</sub><sup>-1</sup> h<sup>-1</sup>, respectively (Fig. 4A). The carbon selectivities of gas, char, and tar are 40.5 %, 34.8 %, and 24.7 %, respectively (Fig. 4B). The  $\eta$  values of rice straw, wheat straw, and corn stalk are 1.65 %, 1.63 %, and 1.64 %, respectively (Fig. 4C). These results show that Ni/Ca<sub>1/8</sub>-SiO<sub>2</sub> also exhibits good performance in light-driven steam biomass reforming.

### 3.3. Roles of H<sub>2</sub>O and Ca<sup>2+</sup>

To reveal the role of H<sub>2</sub>O in the cellulose steam reforming, an isotope labeling test of cellulose reacts with H<sub>2</sub><sup>18</sup>O on Ni/Ca<sub>1/8</sub>-SiO<sub>2</sub> was performed. CO and CO<sub>2</sub> produced in the reaction were analyzed by FTIR. The peaks around 2358, 2343, and 2324 cm<sup>-1</sup> correspond to the C–O stretching modes of C<sup>16</sup>O<sub>2</sub>, C<sup>16</sup>O<sup>18</sup>O, and C<sup>18</sup>O<sub>2</sub>, respectively (Fig. 5A). The two peaks around 2168 and 2116 cm<sup>-1</sup> represent the C–O stretching modes of C<sup>16</sup>O, while the other two peaks around 2127 and 2076 cm<sup>-1</sup> represent those of C<sup>18</sup>O (Fig. 5A). The presence of <sup>18</sup>O in the produced CO and CO<sub>2</sub> shows that H<sub>2</sub>O participates in cellulose reforming.

To investigate the impact of H<sub>2</sub>O on the reaction, we performed dry cellulose pyrolysis on Ni/Ca<sub>1/8</sub>-SiO<sub>2</sub> and Ni/SiO<sub>2</sub> under focused UV-vis-IR illumination. After reacting for 9 min, the production rates of H<sub>2</sub>, CO, CH<sub>4</sub>, and CO<sub>2</sub> are 1485.7, 860.6, 11.7, and 413.1 mmol g<sub>catalyst</sub><sup>-1</sup>

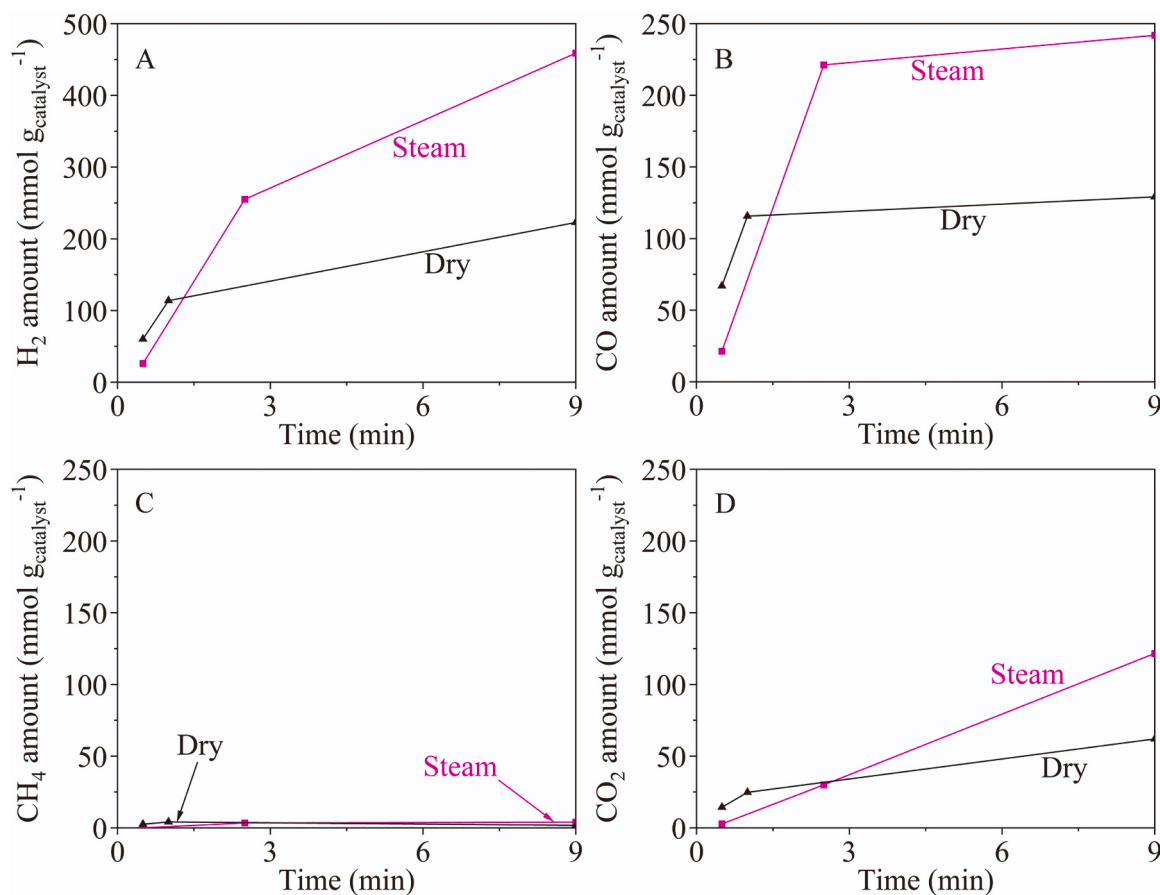


**Fig. 7.** Amounts of H<sub>2</sub> (A), CO (B), CH<sub>4</sub> (C), and CO<sub>2</sub> (D) produced by steam cellulose reforming or dry cellulose pyrolysis on Ni/Ca<sub>1/8</sub>-SiO<sub>2</sub> for specific times under focused UV-vis-IR illumination.

h<sup>-1</sup>, respectively (Fig. 5B) for dry cellulose pyrolysis on Ni/Ca<sub>1/8</sub>-SiO<sub>2</sub>. For Ni/SiO<sub>2</sub>, the production rates of H<sub>2</sub>, CO, CH<sub>4</sub>, and CO<sub>2</sub> are 1425.8, 788.6, 16.0, and 428.8 mmol g<sub>catalyst</sub><sup>-1</sup> h<sup>-1</sup>, respectively (Fig. 5B). The carbon selectivities for gas, char and tar of Ni/Ca<sub>1/8</sub>-SiO<sub>2</sub> are 34.7 %, 9.1 %, and 56.2 %, while those of Ni/SiO<sub>2</sub> are 33.3 %, 15.3 %, and 51.4 %, respectively (Fig. 5C). The  $\eta$  values of cellulose pyrolysis on Ni/Ca<sub>1/8</sub>-SiO<sub>2</sub> and Ni/SiO<sub>2</sub> are 2.5 %, and 2.3 % (Fig. 5D), respectively. Compared to steam cellulose reforming, the hydrogen-rich syngas production rate and  $\eta$  of dry cellulose pyrolysis significantly decrease (Figs. 2A and 5B). On the other hand, there is a noticeable increase in the selectivity of tar for dry cellulose pyrolysis in contrast to steam cellulose reforming (Figs. 2B and 5C). These results indicate that the presence of H<sub>2</sub>O significantly improves the production of hydrogen-rich syngas and dramatically reduces the selectivity of tar.

To investigate the mechanism of H<sub>2</sub>O participating in the reaction on Ni/Ca<sub>1/8</sub>-SiO<sub>2</sub>, steam cellulose reforming and dry cellulose pyrolysis for specific times were conducted. When the C–H bonds in the residue disappear after the reaction, it can be inferred that cellulose has been absolutely pyrolyzed into char. As shown in Fig. 6A and B, the FTIR spectra of the residual solid indicate that the disappearance of C–H stretching peak of cellulose around 2906 cm<sup>-1</sup> takes about 2.5 min during steam cellulose reforming, while in dry cellulose pyrolysis, it only takes about 1 min. After reacting on Ni/Ca<sub>1/8</sub>-SiO<sub>2</sub> for 2.5 min, the carbon selectivities of gas, char, and tar are 45.8 %, 30.0 % and 24.2 %, respectively (Fig. 6C). After dry cellulose pyrolysis on Ni/Ca<sub>1/8</sub>-SiO<sub>2</sub> for 1 min, those are 26.0 %, 20.6 %, and 53.4 %, respectively (Fig. 6C). Combined with the carbon selectivities of steam cellulose reforming (Fig. 2B) and dry cellulose pyrolysis (Fig. 5C) on Ni/Ca<sub>1/8</sub>-SiO<sub>2</sub> for 9 min, it can be observed that selectivity of tar barely changes after the disappearance of C–H bonds. The participation of H<sub>2</sub>O before the

disappearance of C–H bonds considerably promotes the conversion of cellulose to char and decreases the selectivity of tar. Since cellulose is essentially insoluble in H<sub>2</sub>O, the result is caused by the reaction on the surface of Ni nanoparticles of H<sub>2</sub>O with the carbon-containing intermediates from the cellulose pyrolysis. In addition, a significant decrease in char is observed after C–H bonds disappear during steam cellulose reforming. This observation suggests H<sub>2</sub>O can react with char to increase hydrogen-rich syngas production. A decrease of char can also be observed during dry cellulose pyrolysis on Ni/Ca<sub>1/8</sub>-SiO<sub>2</sub> due to the reaction between char with the H<sub>2</sub>O generated by cellulose pyrolysis.

As shown in Fig. 7, the gas amounts produced by steam cellulose reforming and dry cellulose pyrolysis on Ni/Ca<sub>1/8</sub>-SiO<sub>2</sub> for specific times under focused UV-vis-IR illumination were recorded. The production of hydrogen-rich syngas increases rapidly before C–H bonds disappear due to cellulose pyrolysis and the reaction of carbon-containing intermediates with H<sub>2</sub>O. After C–H bonds disappear, hydrogen-rich syngas is primarily produced by char reacting with H<sub>2</sub>O. The increase of CO is almost negligible after C–H bonds disappear, attributed to the WGSR.

In summary, on the one hand, H<sub>2</sub>O can react with the carbon-containing intermediates generated by cellulose pyrolysis to increase the production of char and hydrogen-rich syngas while decreasing tar generation. On the other hand, once cellulose has entirely converted to char, H<sub>2</sub>O can further increase hydrogen-rich syngas production, especially H<sub>2</sub> production, by reacting with the char.

Interestingly, although Ni/Ca<sub>1/8</sub>-SiO<sub>2</sub> exhibits no advantages in dry cellulose pyrolysis for 9 min under focused UV-vis-IR illumination (Fig. 5), it performs much better than Ni/SiO<sub>2</sub> in steam cellulose reforming (Fig. 2). Thus, Ca<sup>2+</sup> ions may significantly improve the performance of Ni/Ca<sub>1/8</sub>-SiO<sub>2</sub> by enhancing the adsorption of H<sub>2</sub>O and promoting the participation of H<sub>2</sub>O in steam cellulose reforming. To

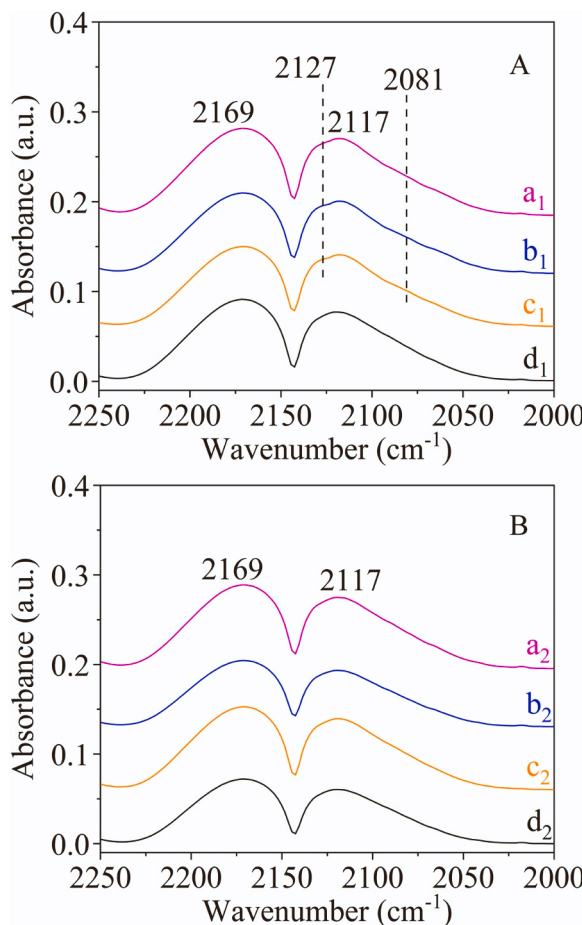


**Fig. 8.** FTIR spectra of CO produced by the reaction between cellulose and  $\text{H}_2^{18}\text{O}$  pre-adsorbed on  $\text{Ni/Ca}_{1/8}\text{-SiO}_2$  (A) and  $\text{Ni/SiO}_2$  (B) after reduction in a flow of 5 vol%  $\text{H}_2/\text{Ar}$  at  $400\text{ }^\circ\text{C}$  ( $a_1$ ,  $a_2$ ),  $200\text{ }^\circ\text{C}$  ( $b_1$ ,  $b_2$ ), after drying at  $70\text{ }^\circ\text{C}$  ( $c_1$ ,  $c_2$ ), and CO produced by the reaction between cellulose and  $\text{H}_2^{16}\text{O}$  adsorbed on  $\text{Ni/Ca}_{1/8}\text{-SiO}_2$  after drying at  $70\text{ }^\circ\text{C}$  ( $d_1$ ,  $d_2$ ).

investigate whether  $\text{Ca}^{2+}$  ions play a vital role in the reaction, we also conducted steam cellulose reforming and dry cellulose pyrolysis on  $\text{Ni/SiO}_2$  in the same conditions as  $\text{Ni/Ca}_{1/8}\text{-SiO}_2$ . As shown in Fig. S9A and S9B, the FTIR spectra of residual solid indicate that the disappearance of C–H bonds in reaction on  $\text{Ni/SiO}_2$  takes the same time as on  $\text{Ni/Ca}_{1/8}\text{-SiO}_2$ . Compared with dry pyrolysis for 1 min, there are apparent differences in the carbon selectivities between  $\text{Ni/SiO}_2$  and  $\text{Ni/Ca}_{1/8}\text{-SiO}_2$  after steam cellulose reforming for 2.5 min (Fig. 6C and S9C). Before the disappearance of C–H bonds, char formation is accelerated during steam cellulose reforming on  $\text{Ni/Ca}_{1/8}\text{-SiO}_2$ , while tar production is decreased. Furthermore, by comparing the carbon selectivities of steam cellulose reforming on  $\text{Ni/Ca}_{1/8}\text{-SiO}_2$  or  $\text{Ni/SiO}_2$  for 2.5 and 9 min (Figs. 6C, 2C, and S9C), it is observed that the consumption of char is much more pronounced on  $\text{Ni/Ca}_{1/8}\text{-SiO}_2$ . This suggests that  $\text{Ca}^{2+}$  doping promotes the reaction of char with  $\text{H}_2\text{O}$  on the other hand.

We also recorded the gas amounts produced during steam cellulose reforming and dry cellulose pyrolysis on  $\text{Ni/SiO}_2$  for specific times. As shown in Fig. S10, the hydrogen-rich syngas production of steam cellulose reforming on  $\text{Ni/SiO}_2$  is significantly reduced whether before or after the disappearance of C–H bonds compared to the reaction on  $\text{Ni/Ca}_{1/8}\text{-SiO}_2$  (Fig. 7). However, the amounts of hydrogen-rich syngas produced by dry cellulose pyrolysis on the two catalysts are similar. The results demonstrate that the excellent performance of  $\text{Ni/Ca}_{1/8}\text{-SiO}_2$  comes from enhancing the adsorption and participation of  $\text{H}_2\text{O}$  in the reaction by  $\text{Ca}^{2+}$  ions.

To confirm the enhancement of  $\text{H}_2\text{O}$  adsorption by  $\text{Ca}^{2+}$  doping in

$\text{Ni/Ca}_{1/8}\text{-SiO}_2$ , we performed another isotope labeling experiment of cellulose reforming with  $\text{H}_2^{18}\text{O}$  pre-adsorbed on  $\text{Ni/Ca}_{1/8}\text{-SiO}_2$  and  $\text{Ni/SiO}_2$ . As shown in Fig. 8A, for the reaction between cellulose and  $\text{H}_2^{18}\text{O}$  pre-adsorbed on  $\text{Ni/Ca}_{1/8}\text{-SiO}_2$ ,  $\text{C}^{18}\text{O}$  peaks still exist though the catalyst has been reduced in a flow of 5 vol%  $\text{H}_2/\text{Ar}$  at  $400\text{ }^\circ\text{C}$  for 0.5 h. While for  $\text{Ni/SiO}_2$ , no  $\text{C}^{18}\text{O}$  peaks are observed though the catalyst is just dried at  $70\text{ }^\circ\text{C}$  for 12 h (Fig. 8B). That is to say, neither  $\text{Ni}$  nanoparticles nor  $\text{SiO}_2$  support has strong adsorption of  $\text{H}_2\text{O}$ . The results demonstrate that the presence of  $\text{Ca}^{2+}$  ions dramatically enhances the adsorption of  $\text{H}_2\text{O}$  on  $\text{Ni/Ca}_{1/8}\text{-SiO}_2$ , thus significantly improving catalytic activity as compared to  $\text{Ni/SiO}_2$ .

### 3.4. Roles of light

#### 3.4.1. Heating effect

Due to the strong absorption over the whole solar spectrum (Fig. 9A), the surface temperature of  $\text{Ni/Ca}_{1/8}\text{-SiO}_2$  and  $\text{Ni/SiO}_2$  will rise rapidly under focused UV-vis-IR illumination to which thermocatalytic steam cellulose reforming can be triggered. As the reaction progressed, the cellulose quickly coked, and the temperature of the reactant reached an equilibrium point. The surface temperature of the reactant was measured. As shown in the temperature evolution of the catalyst and cellulose mixture with the time of focused illumination (Fig. S11), the equilibrium temperature of steam cellulose reforming on  $\text{Ni/SiO}_2$  under focused UV-vis-IR illumination is  $700\text{ }^\circ\text{C}$  (Fig. 9B). For the reaction on  $\text{Ni/Ca}_{1/8}\text{-SiO}_2$  under focused UV-vis-IR,  $\lambda > 420\text{ nm}$ , and  $\lambda > 560\text{ nm}$  vis-IR, the equilibrium temperatures are  $693\text{ }^\circ\text{C}$ ,  $629\text{ }^\circ\text{C}$ , and  $594\text{ }^\circ\text{C}$ , respectively (Fig. 9B). To verify whether the strong absorption over the whole solar spectrum of  $\text{Ni/Ca}_{1/8}\text{-SiO}_2$  causes photocatalytic activity, steam cellulose reforming on  $\text{Ni/Ca}_{1/8}\text{-SiO}_2$  under UV-vis-IR illumination was conducted at near RT. After illuminating for 30 min, no  $\text{CO}$  or  $\text{H}_2$  was detected (Fig. S12). Therefore, the high catalytic activity of  $\text{Ni/Ca}_{1/8}\text{-SiO}_2$  is primarily ascribed to light-driven thermocatalysis rather than photocatalysis.

#### 3.4.2. Photoactivation

Does the excellent catalytic performance of  $\text{Ni/Ca}_{1/8}\text{-SiO}_2$  merely derive from the thermocatalysis? To address this inquiry, the reaction on  $\text{Ni/Ca}_{1/8}\text{-SiO}_2$  was conducted in a fixed bed at varying temperatures with illumination or in the dark (Scheme S3). With UV-vis-IR,  $\lambda > 420\text{ nm}$ , and  $\lambda > 560\text{ nm}$  vis-IR illumination, the initial temperatures for  $\text{H}_2$  formation are  $150\text{ }^\circ\text{C}$ ,  $200\text{ }^\circ\text{C}$ , and  $250\text{ }^\circ\text{C}$ , respectively, while in the dark, it increases to  $450\text{ }^\circ\text{C}$  (Fig. 9C). For  $\text{CO}$  formation, the initial temperatures with UV-vis-IR,  $\lambda > 420\text{ nm}$  vis-IR, and  $\lambda > 560\text{ nm}$  vis-IR illumination are  $100\text{ }^\circ\text{C}$ ,  $150\text{ }^\circ\text{C}$ , and  $200\text{ }^\circ\text{C}$ , respectively, while in the dark it is  $250\text{ }^\circ\text{C}$  (Fig. 9D). These results indicate the significant effect of illumination in reducing the initial formation temperature of the hydrogen-rich syngas. Additionally, compared to the reaction in the dark, the amount of hydrogen-rich syngas produced with illumination is much higher. The absence of photocatalytic activity on  $\text{Ni/Ca}_{1/8}\text{-SiO}_2$  (Fig. S12) suggests a photoactivation effect of illumination in addition to the heating effect, thus improving the activity of  $\text{Ni/Ca}_{1/8}\text{-SiO}_2$ .

### 3.5. The origin of photoactivation

To further understand the photoactivation, the effect of illumination on dry cellulose pyrolysis on  $\text{Ni/Ca}_{1/8}\text{-SiO}_2$  at varying temperatures was conducted (Scheme S3). With UV-vis-IR illumination, the initial formation temperatures of  $\text{H}_2$  and  $\text{CO}$  are  $200\text{ }^\circ\text{C}$  and  $100\text{ }^\circ\text{C}$ , respectively, while in the dark, these temperatures increase to  $325\text{ }^\circ\text{C}$  and  $275\text{ }^\circ\text{C}$ , respectively (Fig. 10A and B). In addition, the final  $\text{H}_2$  and  $\text{CO}$  amounts at  $700\text{ }^\circ\text{C}$  of cellulose pyrolysis with illumination are  $129.2$  and  $80.0\text{ mmol g}_{\text{catalyst}}^{-1}$ , respectively, while in the dark, these amounts decrease to  $73.4$  and  $35.4\text{ mmol g}_{\text{catalyst}}^{-1}$ , respectively (Fig. 10A and B). The results suggest that illumination accelerates the dry cellulose pyrolysis on  $\text{Ni/Ca}_{1/8}\text{-SiO}_2$ . Since solid-solid contact prevents the catalyst

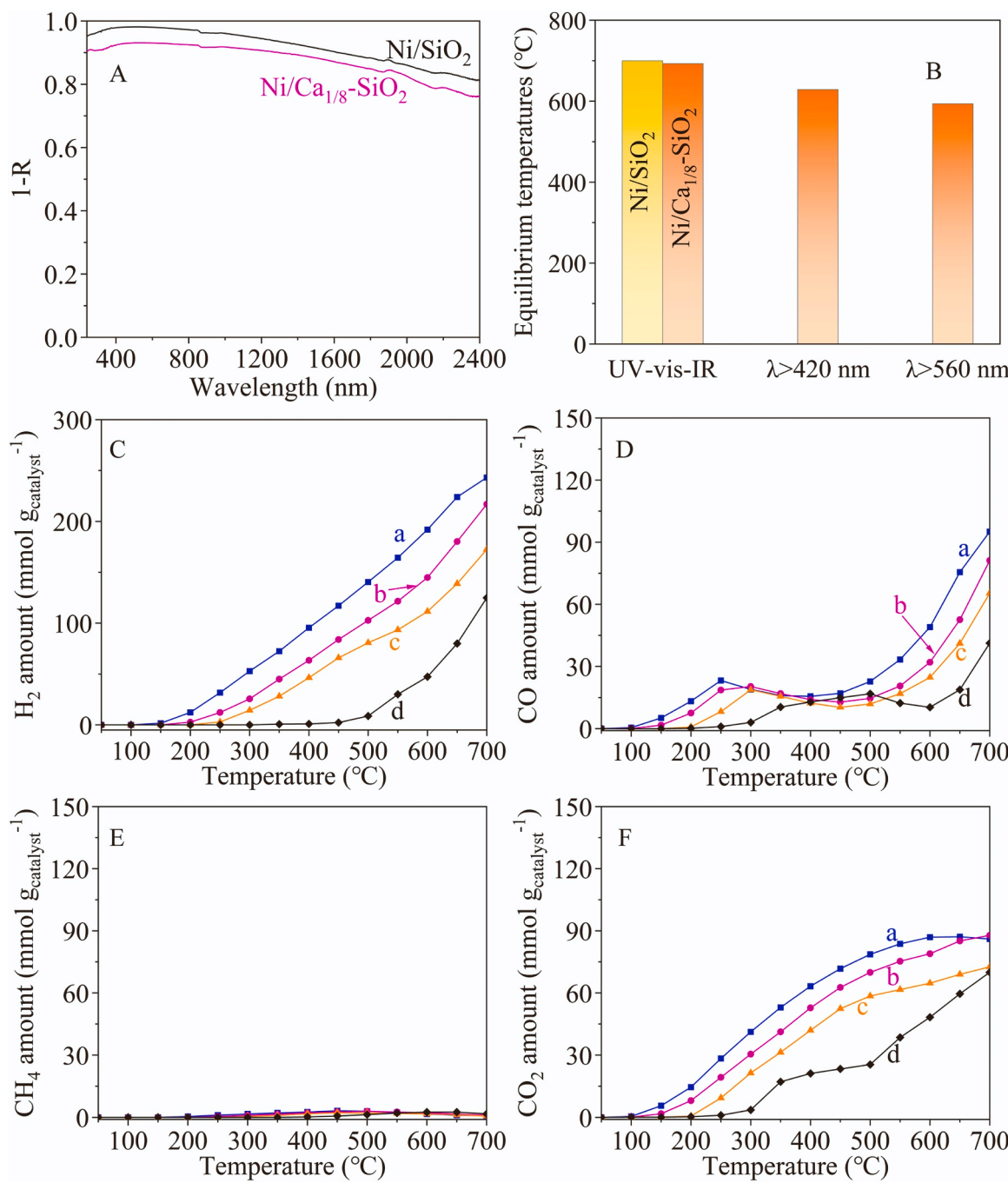


**Fig. 9.** Diffusive reflectance spectrum (A) of  $\text{Ni}/\text{Ca}_{1/8}\text{-SiO}_2$  and  $\text{Ni}/\text{SiO}_2$ . Equilibrium temperatures (B) of  $\text{Ni}/\text{Ca}_{1/8}\text{-SiO}_2$  and  $\text{Ni}/\text{SiO}_2$  under focused illumination. The amounts of  $\text{H}_2$  (C),  $\text{CO}$  (D),  $\text{CH}_4$  (E), and  $\text{CO}_2$  (F) produced by steam cellulose reforming on  $\text{Ni}/\text{Ca}_{1/8}\text{-SiO}_2$  at varying temperatures in fixed bed with UV-vis-IR (a),  $\lambda > 420 \text{ nm}$  (b), and  $\lambda > 560 \text{ nm}$  (c) vis-IR illumination or in the dark (d).

from effectively participating in cellulose pyrolysis, the photoactivation observed in the reaction should be ascribed to promote adsorbed  $\text{H}_2\text{O}$  from cellulose pyrolysis participating in the reaction. To determine the origin of photoactivation during dry cellulose pyrolysis on  $\text{Ni}/\text{Ca}_{1/8}\text{-SiO}_2$ , the reaction was also conducted on  $\text{Ni}/\text{SiO}_2$ . As shown in Fig. S13, dry cellulose pyrolysis on  $\text{Ni}/\text{SiO}_2$  shows little difference between with illumination and in the dark. Moreover, although  $\text{Ni}/\text{Ca}_{1/8}\text{-SiO}_2$  exhibits better performance than  $\text{Ni}/\text{SiO}_2$  in the reaction with illumination, their performance in the dark is almost the same. This demonstrates that the photoactivation during the dry cellulose pyrolysis on  $\text{Ni}/\text{Ca}_{1/8}\text{-SiO}_2$  should be ascribed to promote the adsorbed  $\text{H}_2\text{O}$  from cellulose pyrolysis participating in the reaction.

In contrast to dry cellulose pyrolysis in a fixed bed with illumination (Scheme S3),  $\text{Ni}/\text{Ca}_{1/8}\text{-SiO}_2$  does not perform better than  $\text{Ni}/\text{SiO}_2$  during the dry cellulose pyrolysis in the stainless-steel reactor (Scheme S1) under focused UV-vis-IR illumination (Figs. 5, 7, and S10). This is attributed to the fact that the heating rate under focused UV-vis-IR illumination is too fast for  $\text{H}_2\text{O}$  from cellulose pyrolysis to adsorb on the catalysts, and the vacuum condition aggravates the difficulty of  $\text{H}_2\text{O}$  adsorption. To verify the conclusion, steam cellulose reforming was also conducted on  $\text{Ni}/\text{SiO}_2$  at varying temperatures in a fixed bed with illumination or in the dark. As shown in Fig. S14, little difference can be observed in the reaction on  $\text{Ni}/\text{SiO}_2$  in the dark compared to  $\text{Ni}/\text{Ca}_{1/8}\text{-SiO}_2$  (Fig. 10). Nevertheless, with illumination, the performance of  $\text{Ni}/\text{SiO}_2$

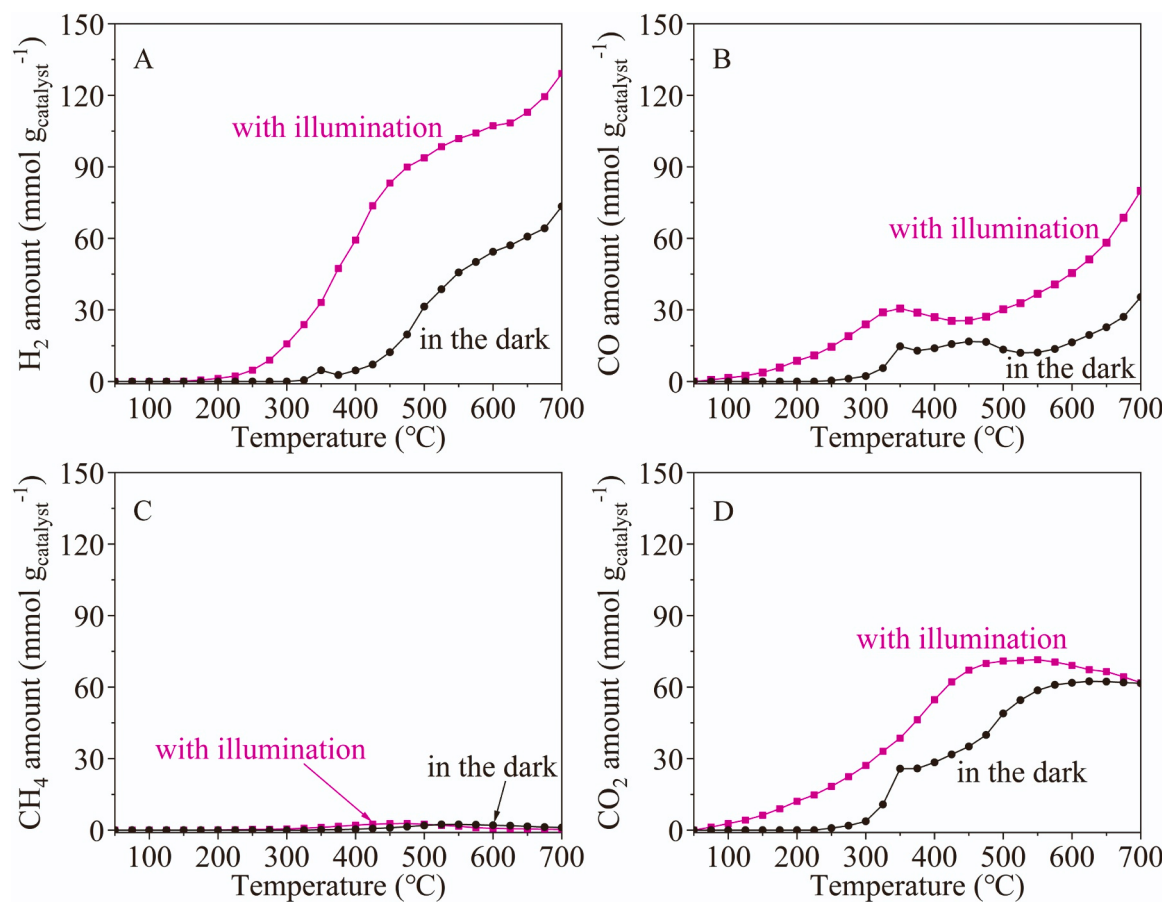


**Fig. 10.** Amounts of H<sub>2</sub> (A), CO (B), CH<sub>4</sub> (C), and CO<sub>2</sub> (D) produced by dry cellulose pyrolysis on Ni/Ca<sub>1/8</sub>-SiO<sub>2</sub> at varying temperatures in fixed bed with UV-vis-IR illumination or in the dark.

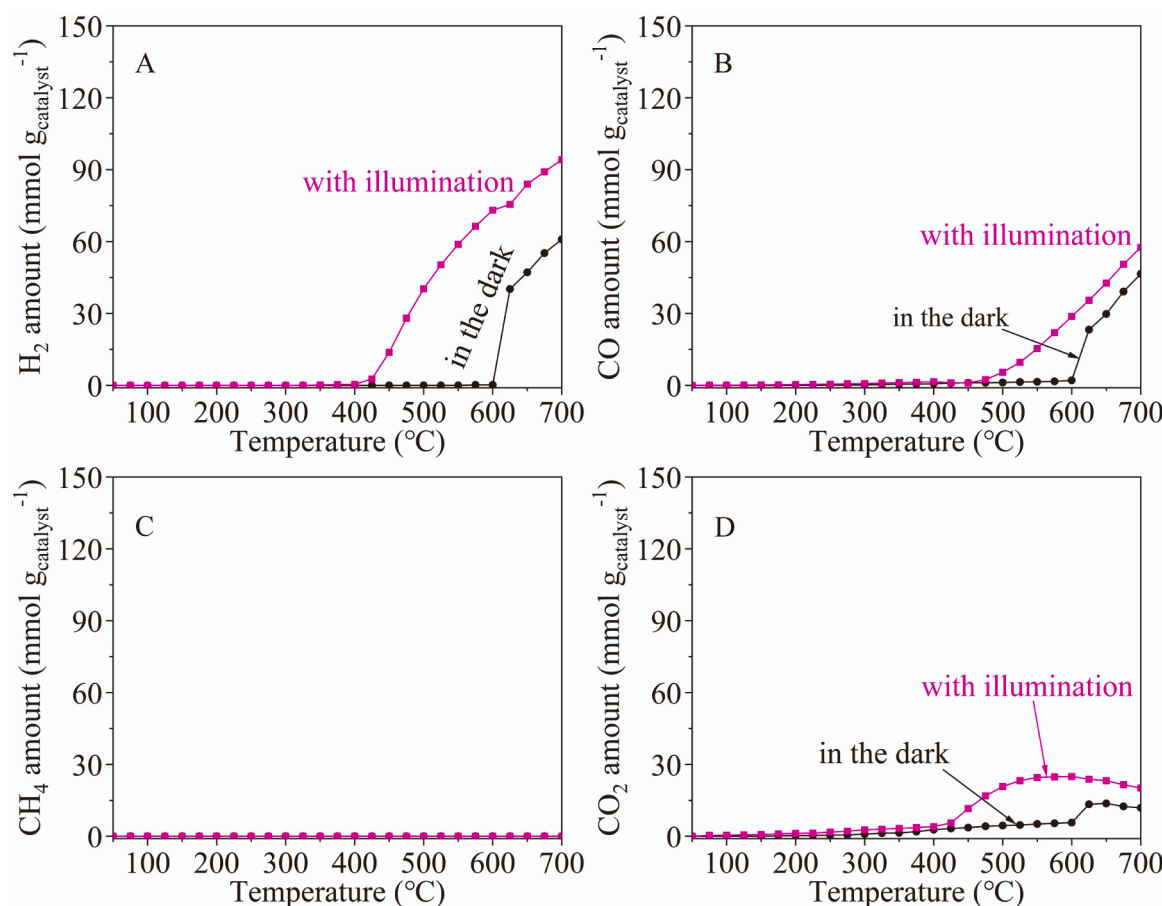
Ca<sub>1/8</sub>-SiO<sub>2</sub> is considerably better than Ni/SiO<sub>2</sub>. Since the adsorption of H<sub>2</sub>O on Ni/Ca<sub>1/8</sub>-SiO<sub>2</sub> is much stronger than Ni/SiO<sub>2</sub>, these results verify that light promotes the reactions between the intermediate species (by cellulose pyrolysis) and the strongly adsorbed H<sub>2</sub>O on Ca<sup>2+</sup> doped SiO<sub>2</sub> for Ni/Ca<sub>1/8</sub>-SiO<sub>2</sub>.

Our previous work has shown that the C\* species oxidation by O\* on Ni nanoparticles is the rate-determining step [37]. In this study, the effect of illumination on pre-formed char reacting with adsorbed H<sub>2</sub>O on Ni/Ca<sub>1/8</sub>-SiO<sub>2</sub> in a fixed bed was also investigated (Scheme S3 and S4). With illumination, the initial temperature of H<sub>2</sub> formation is 400 °C, while in the dark, it increases to 600 °C (Figs. 11A and 11B). The final H<sub>2</sub> and CO amounts at 700 °C with illumination are 94.1 and 57.6 mmol g<sub>catalyst</sub><sup>-1</sup>, respectively, whereas in the dark, they are 60.9 and 46.5 mmol g<sub>catalyst</sub><sup>-1</sup>, respectively (Fig. 11A and B). These results suggest that illumination also significantly enhances the reaction of char with adsorbed H<sub>2</sub>O on Ni/Ca<sub>1/8</sub>-SiO<sub>2</sub>. As a comparison, the reaction was also performed on Ni/SiO<sub>2</sub>. With UV-vis-IR illumination, the initial formation temperature of H<sub>2</sub> is 525 °C, while in the dark, it reaches 625 °C (Fig. S15A and S15B). The final H<sub>2</sub> and CO amounts at 700 °C with illumination are 49.2 and 36.3 mmol g<sub>catalyst</sub><sup>-1</sup>, respectively, while in the dark, they are 31.9 and 22.2 mmol g<sub>catalyst</sub><sup>-1</sup>, respectively (Fig. S15A and S15B). As we can see, benefiting from the stronger H<sub>2</sub>O adsorption, Ni/Ca<sub>1/8</sub>-SiO<sub>2</sub> exhibits much better than Ni/SiO<sub>2</sub> during pre-formed char reaction with adsorbed H<sub>2</sub>O, whether with illumination or in the dark.

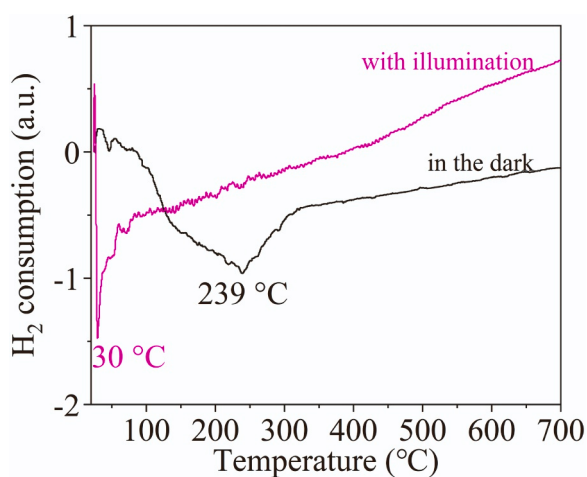
As described in our previous work [37], photoactivation has a negligible impact on the H<sub>2</sub>O dissociation on Ni particles but promotes C\* species oxidation by O\* species. Here, we also investigated how illumination affects the reduction of pre-chemisorbed oxygen on the surface of Ni nanoparticles in Ni/Ca<sub>1/8</sub>-SiO<sub>2</sub> via H<sub>2</sub>-TPR. As depicted in

Fig. 12, with illumination, the peak of H<sub>2</sub> consumption significantly shifts from 239 °C to 30 °C, in contrast to H<sub>2</sub>-TPR in the dark. According to the results, the illumination significantly activates the Ni-O bonds, thus promoting C\* species oxidation by O\* species and enhancing the catalytic performance of Ni/Ca<sub>1/8</sub>-SiO<sub>2</sub>. The light-induced Ni-O activation on the surface of Ni nanoparticles is probably due to the following reason: upon focused illumination, the electrons of Ni nanoparticles are promoted to the excitation states, which weakens the bond of the adsorbed surface oxygen with Ni atoms [37].

Based on the above evidences in Sections 3.3, 3.4 and 3.5, a mechanism of light-driven thermocatalytic steam cellulose reforming on Ni/Ca<sub>1/8</sub>-SiO<sub>2</sub> is proposed in Scheme 1. Steam cellulose reforming on Ni/Ca<sub>1/8</sub>-SiO<sub>2</sub> initiates with cellulose pyrolyzing to carbon-containing intermediates including tar (C<sub>x</sub>H<sub>y</sub>O<sub>z</sub>), H<sub>2</sub>O, syngas, char, etc. Meanwhile, H<sub>2</sub>O molecules are weakly adsorbed on SiO<sub>2</sub> and strongly adsorbed on Ca<sup>2+</sup> ions. They transfer via the Ni/Ca<sub>1/8</sub>-SiO<sub>2</sub> interface to the surface of metallic Ni nanoparticles, where they are dissociated to H\* and O\* (forming Ni-O bonds) species. The C<sub>x</sub>H<sub>y</sub>O<sub>z</sub> including tar is oxidized by O\* species, generating syngas. Char on the surface of Ni nanoparticles also reacts with O\* species to produce CO. Due to the side-reaction of WGSR, a portion of CO is oxidized by O\* species to be CO<sub>2</sub>, promoting H<sub>2</sub> production, thus leading to the amount of H<sub>2</sub> much higher than CO. Compared to the reactions on Ni/SiO<sub>2</sub> where only H<sub>2</sub>O molecules are weakly adsorbed on SiO<sub>2</sub>, the strongly adsorbed H<sub>2</sub>O molecules on Ca<sup>2+</sup> ions for Ni/Ca<sub>1/8</sub>-SiO<sub>2</sub> substantially promote the oxidation of both C<sub>x</sub>H<sub>y</sub>O<sub>z</sub> and char, thus significantly enhancing syngas production rates and decreasing the char and tar selectivities. Light can promote the oxidation of carbon species by O\* species chemisorbed on the surface of Ni nanoparticles due to the surface Ni-O bonds being activated upon light illumination, thus significantly facilitating the reactions.



**Fig. 11.** The amounts of H<sub>2</sub> (A), CO (B), CH<sub>4</sub> (C), and CO<sub>2</sub> (D) produced by pre-formed char reacting with adsorbed H<sub>2</sub>O on Ni/Ca<sub>1/8</sub>-SiO<sub>2</sub> at varying temperatures in fixed bed with UV-vis-IR illumination or in the dark.



**Fig. 12.** H<sub>2</sub>-TPR profiles of Ni/Ca<sub>1/8</sub>-SiO<sub>2</sub> after pre-chemisorbing oxygen on Ni nanoparticles with UV-vis-IR illumination and in the dark.

#### 4. Conclusion

In summary, we synthesize a catalyst of Ni nanoparticles loading on Ca<sup>2+</sup> doped SiO<sub>2</sub>. The catalyst shows a high hydrogen-rich syngas production rate and good durability for light-driven thermocatalytic steam cellulose reforming merely under focused UV-vis-IR illumination. The participation of H<sub>2</sub>O substantially decreases tar selectivity, increasing hydrogen-rich syngas production. Ca<sup>2+</sup> doping enhances H<sub>2</sub>O

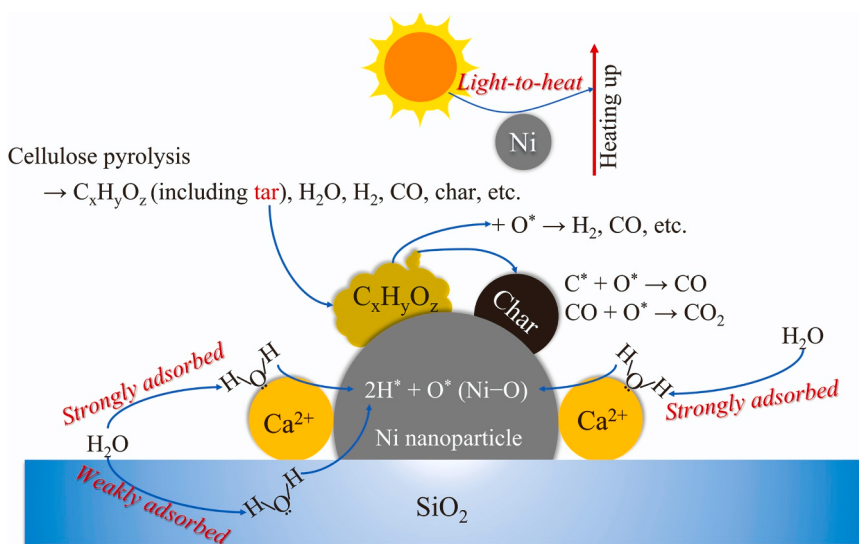
adsorption, thus promoting the participation of H<sub>2</sub>O in the reaction. Light not only act as a heating role, but also significantly promotes the reaction between carbon species (produced by cellulose pyrolysis) and the strongly adsorbed H<sub>2</sub>O on Ca<sup>2+</sup> doped silica due to oxygen chemisorbed on the surface of Ni nanoparticles being activated upon illumination, thus facilitating the cellulose reforming. The present strategy of loading Ni nanoparticles on SiO<sub>2</sub> doped by Ca<sup>2+</sup> ions can be applied to design catalysts for effectively reducing tar production while maintaining excellent activity and durability during light-driven thermocatalytic steam biomass reforming.

#### CRediT authorship contribution statement

**Jichun Wu:** Conceptualization, Investigation, Methodology, Writing – original draft. **Yuanzhi Li:** Conceptualization, Funding acquisition, Methodology, Writing – review & editing. **Chongyang Zhou:** Conceptualization, Methodology. **Qianqian Hu:** Methodology, Writing – review & editing. **Mengqi Zhong:** Methodology, Writing – review & editing. **Huamin Cao:** Methodology, Writing – review & editing. **Yaqi Hu:** Methodology, Writing – review & editing. **Lei Ji:** Methodology, Writing – review & editing.

#### Declaration of Competing Interest

The authors declare that they have no known competing financial interests or personal relationships that could have appeared to influence the work reported in this paper.



**Scheme 1.** Schematically illustrated mechanism of light-driven thermocatalytic steam cellulose reforming on  $\text{Ni}/\text{Ca}_{1/8}\text{-SiO}_2$ .

## Data Availability

Data will be made available on request.

## Acknowledgement

This work was supported by National Natural Science Foundation of China (21972109).

## Appendix A. Supporting information

Supplementary data associated with this article can be found in the online version at [doi:10.1016/j.apcatb.2023.123388](https://doi.org/10.1016/j.apcatb.2023.123388).

## References

- [1] A.S. Al-Fatesh, Y. Arafat, S.O. Kasim, A.A. Ibrahim, A.E. Abasaeed, A.H. Fakheeha, In situ auto-gasification of coke deposits over a novel Ni-Ce/W-Zr catalyst by sequential generation of oxygen vacancies for remarkably stable syngas production via  $\text{CO}_2$ -reforming of methane, *Appl. Catal. B-Environ.* 280 (2021), 119445, <https://doi.org/10.1016/j.apcatb.2020.119445>.
- [2] K. Han, Y. Wang, S. Wang, Q. Liu, Z. Deng, F. Wang, Narrowing band gap energy of  $\text{CeO}_2$  in  $(\text{Ni}/\text{CeO}_2)/\text{SiO}_2$  catalyst for photothermal methane dry reforming, *Chem. Eng. J.* 421 (2021), 129989, <https://doi.org/10.1016/j.cej.2021.129989>.
- [3] A.A. Khan, M. Tahir, Well-designed 2D/2D  $\text{Ti}_3\text{C}_2\text{T}_{\text{A/R}}$  MXene coupled g-C<sub>3</sub>N<sub>4</sub> heterojunction with in-situ growth of anatase/rutile  $\text{TiO}_2$  nucleates to boost photocatalytic dry-reforming of methane (DRM) for syngas production under visible light, *Appl. Catal. B-Environ.* 285 (2021), 119777, <https://doi.org/10.1016/j.apcatb.2020.119777>.
- [4] Y.F. Xu, X.Y. Li, J.H. Gao, J. Wang, G.Y. Ma, X.D. Wen, Y. Yang, Y.W. Li, M.Y. Ding, A hydrophobic FeMn@Si catalyst increases olefins from syngas by suppressing C1 by-products, *Science* 371 (2021) 610–613, <https://doi.org/10.1126/science.abb3649>.
- [5] I.V. Yentekakis, P. Panagiotopoulou, G. Artemakis, A review of recent efforts to promote dry reforming of methane (DRM) to syngas production via bimetallic catalyst formulations, *Appl. Catal. B-Environ.* 296 (2021), 120210, <https://doi.org/10.1016/j.apcatb.2021.120210>.
- [6] C. Mora, T. McKenzie, J.M. Gaw, J.M. Dean, H. von Hammerstein, T.A. Knudson, R. O. Setter, C.Z. Smith, K.M. Webster, J.A. Patz, E.C. Franklin, Over half of known human pathogenic diseases can be aggravated by climate change, *Nat. Clim. Change* 12 (2022) 869–875, <https://doi.org/10.1038/s41558-022-01426-1>.
- [7] D. Zhong, Z. Chang, K. Zeng, J. Li, Y. Qiu, Q. Lu, G. Flamant, H. Yang, H. Chen, Solar pyrolysis of biomass - part I: volatile evolution mechanism, *Energy Conv. Manag.* 267 (2022), 115951, <https://doi.org/10.1016/j.enconman.2022.115951>.
- [8] A. Curcio, S. Rodat, V. Vuillerme, S. Abanades, Design and validation of reactant feeding control strategies for the solar-autothermal hybrid gasification of woody biomass, *Energy* 254 (2022), 124481, <https://doi.org/10.1016/j.energy.2022.124481>.
- [9] N. García-Gómez, J. Vallecillos, A. Remiro, B. Valle, J. Bilbao, A.G. Gayubo, Effect of reaction conditions on the deactivation by coke of a  $\text{NiAl}_2\text{O}_4$  spinel derived catalyst in the steam reforming of bio-oil, *Appl. Catal. B-Environ.* 297 (2021), 120445, <https://doi.org/10.1016/j.apcatb.2021.120445>.
- [10] A.D. Lalsare, B. Leonard, B. Robinson, A.C. Sivri, R. Vukmanovich, C. Dumitrescu, W. Rogers, J. Hu, Self-regenerable carbon nanofiber supported Fe –  $\text{Mo}_2\text{C}$  catalyst for  $\text{CH}_4\text{-CO}_2$  assisted reforming of biomass to hydrogen rich syngas, *Appl. Catal. B-Environ.* 282 (2021), 119537, <https://doi.org/10.1016/j.apcatb.2020.119537>.
- [11] S. Valizadeh, S.-H. Jang, G. Hoon Rhee, J. Lee, P. Loke Show, M. Ali Khan, B.-H. Jeon, K.-Y. Andrew Lin, C. Hyun Ko, W.-H. Chen, Y.-K. Park, Biohydrogen production from furniture waste via catalytic gasification in air over Ni-loaded ultra-stable Y-type zeolite, *Chem. Eng. J.* 433 (2022), 133793, <https://doi.org/10.1016/j.cej.2021.133793>.
- [12] J. Wang, B. Zhao, S. Liu, D. Zhu, F. Huang, H. Yang, H. Guan, A. Song, D. Xu, L. Sun, H. Xie, W. Wei, W. Zhang, T. Helmer Pedersen, Catalytic pyrolysis of biomass with Ni/Fe-CaO-based catalysts for hydrogen-rich gas: DFT and experimental study, *Energy Conv. Manag.* 254 (2022), 115246, <https://doi.org/10.1016/j.enconman.2022.115246>.
- [13] X. Yang, S. Gu, A. Kheradmand, T. Kan, J. He, V. Strezov, R. Zou, A. Yu, Y. Jiang, Tunable syngas production from biomass: synergistic effect of steam, Ni–CaO catalyst, and biochar, *Energy* 254 (2022), 123904, <https://doi.org/10.1016/j.energy.2022.123904>.
- [14] G. Kong, X. Zhang, K. Wang, L. Zhou, J. Wang, X. Zhang, L. Han, Tunable  $\text{H}_2/\text{CO}$  syngas production from co-gasification integrated with steam reforming of sewage sludge and agricultural biomass: a experimental study, *Appl. Energy* 342 (2023), 121195, <https://doi.org/10.1016/j.apenergy.2023.121195>.
- [15] L. Ruivo, T. Silva, D. Neves, L. Tarelho, J. Frade, Thermodynamic guidelines for improved operation of iron-based catalysts in gasification of biomass, *Energy* 268 (2023), 126641, <https://doi.org/10.1016/j.energy.2023.126641>.
- [16] J. Seo, H. Kim, S. Jeon, S. Valizadeh, Y. Khani, B.H. Jeon, G.H. Rhee, W.H. Chen, S. Lam, M.A. Khan, Y.K. Park, Thermocatalytic conversion of wood-plastic composite over HZSM-5 catalysts, *Bioresour. Technol.* 373 (2023), 128702, <https://doi.org/10.1016/j.biortech.2023.128702>.
- [17] R. Zou, Z. Chen, L. Zhong, W. Yang, T. Li, J. Gan, Y. Yang, Z. Chen, H. Lai, X. Li, C. Liu, S. Admassie, E.I. Iwuoha, J. Lu, X. Peng, Nanocellulose-assisted molecularly engineering of nitrogen deficient graphitic carbon nitride for selective biomass photo-oxidation, *Adv. Funct. Mater.* 33 (2023), <https://doi.org/10.1002/adfm.202301311>.
- [18] H. Zhao, J. Liu, N. Zhong, S. Larter, Y. Li, M.G. Kibria, B.L. Su, Z. Chen, J. Hu, Biomass photoreforming for hydrogen and value-added chemicals co-production on hierarchically porous photocatalysts, *Adv. Energy Mater.* 13 (2023), <https://doi.org/10.1002/aenm.202300257>.
- [19] Y. Yan, X. Yu, C. Shao, Y. Hu, W. Huang, Y. Li, Atomistic structural engineering of conjugated microporous polymers promotes photocatalytic biomass valorization, *Adv. Funct. Mater.* (2023), <https://doi.org/10.1002/adfm.202304604>.
- [20] C. Shi, F. Kang, Y. Zhu, M. Teng, J. Shi, H. Qi, Z. Huang, C. Si, F. Jiang, J. Hu, Photoreforming lignocellulosic biomass for hydrogen production: optimized design of photocatalyst and photocatalytic system, *Chem. Eng. J.* 452 (2023), 138980, <https://doi.org/10.1016/j.cej.2022.138980>.
- [21] H. Zhang, H. Zhao, S. Zhai, R. Zhao, J. Wang, X. Cheng, H.S. Shiran, S. Larter, M. G. Kibria, J. Hu, Electron-enriched Lewis acid-base sites on red carbon nitride for simultaneous hydrogen production and glucose isomerization, *Appl. Catal. B-Environ.* 316 (2022), 121647, <https://doi.org/10.1016/j.apcatb.2022.121647>.
- [22] Y. Choi, R. Mehrotra, S.H. Lee, T.V.T. Nguyen, I. Lee, J. Kim, H.Y. Yang, H. Oh, H. Kim, J.W. Lee, Y.H. Kim, S.Y. Jang, J.W. Jang, J. Ryu, Bias-free solar hydrogen production at 19.8  $\text{mA cm}^{-2}$  using perovskite photocathode and lignocellulosic biomass, *Nat. Commun.* 13 (2022) 5709, <https://doi.org/10.1038/s41467-022-33435-1>.
- [23] Z. Zhang, M. Wang, H. Zhou, F. Wang, Surface sulfate ion on CdS catalyst enhances syngas generation from biopolymers, *J. Am. Chem. Soc.* 143 (2021) 6533–6541, <https://doi.org/10.1021/jacs.1c00830>.

- [24] L. Wang, R. Tang, A. Kheradmand, Y. Jiang, H. Wang, W. Yang, Z. Chen, X. Zhong, S.P. Ringer, X. Liao, W. Liang, J. Huang, Enhanced solar-driven benzaldehyde oxidation with simultaneous hydrogen production on Pt single-atom catalyst, *Appl. Catal. B-Environ.* 284 (2021), 119759, <https://doi.org/10.1016/j.apcatb.2020.119759>.
- [25] C.Y. Toe, C. Tsounis, J. Zhang, H. Masood, D. Gunawan, J. Scott, R. Amal, Advancing photoreforming of organics: highlights on photocatalyst and system designs for selective oxidation reactions, *Energy Environ. Sci.* 14 (2021) 1140–1175, <https://doi.org/10.1039/d0ee03116j>.
- [26] Y. Li, R. He, P. Han, B. Hou, S. Peng, C. Ouyang, A new concept: volume photocatalysis for efficient H<sub>2</sub> generation – using low polymeric carbon nitride as an example, *Appl. Catal. B-Environ.* 279 (2020), 119379, <https://doi.org/10.1016/j.apcatb.2020.119379>.
- [27] D. Mateo, A. García-Mulero, J. Albero, H. García, N-doped defective graphene decorated by strontium titanate as efficient photocatalyst for overall water splitting, *Appl. Catal. B-Environ.* 252 (2019) 111–119, <https://doi.org/10.1016/j.apcatb.2019.04.011>.
- [28] Y. Choi, S. Choi, I. Lee, T.V.T. Nguyen, S. Bae, Y.H. Kim, J. Ryu, S. Park, J. Ryu, Solar biomass reforming and hydrogen production with earth-abundant Si-based photocatalysts, *Adv. Mater.* (2023), e2301576, <https://doi.org/10.1002/adma.202301576>.
- [29] Y. Xu, L. Wang, Z. Shi, N. Su, C. Li, Y. Huang, N. Huang, Y. Deng, H. Li, T. Ma, X. Y. Kong, W. Lin, Y. Zhou, L. Ye, Peroxide-mediated selective conversion of biomass polysaccharides over high entropy sulfides via solar energy catalysis, *Energy Environ. Sci.* 16 (2023) 1531–1539, <https://doi.org/10.1039/d2ee03357g>.
- [30] Q. Cheng, Y.-J. Yuan, R. Tang, Q.-Y. Liu, L. Bao, P. Wang, J. Zhong, Z. Zhao, Z.-T. Yu, Z. Zou, Rapid hydroxyl radical generation on (001)-facet-exposed ultrathin anatase TiO<sub>2</sub> nanosheets for enhanced photocatalytic lignocellulose-to-H<sub>2</sub> conversion, *ACS Catal.* 12 (2022) 2118–2125, <https://doi.org/10.1021/acscatal.1c05713>.
- [31] H. Zhao, C.-F. Li, X. Yu, N. Zhong, Z.-Y. Hu, Y. Li, S. Larter, M.G. Kibria, J. Hu, Mechanistic understanding of cellulose  $\beta$ -1,4-glycosidic cleavage via photocatalysis, *Appl. Catal. B-Environ.* 302 (2022), 120872, <https://doi.org/10.1016/j.apcatb.2021.120872>.
- [32] V.-C. Nguyen, D.B. Nimbalkar, L.D. Nam, Y.-L. Lee, H. Teng, Photocatalytic cellulose reforming for H<sub>2</sub> and formate production by using graphene oxide-dot catalysts, *ACS Catal.* 11 (2021) 4955–4967, <https://doi.org/10.1021/acscatal.1c00217>.
- [33] D.W. Wakerley, M.F. Kuehnle, K.L. Orchard, K.H. Ly, T.E. Rosser, E. Reisner, Solar-driven reforming of lignocellulose to H<sub>2</sub> with a CdS/CdO<sub>x</sub> photocatalyst, *Nat. Energy* 2 (2017) 17021, <https://doi.org/10.1038/nenergy.2017.21>.
- [34] D. Aboagye, R. Djellabi, F. Medina, S. Contreras, Radical-mediated photocatalysis for lignocellulosic biomass conversion into value-added chemicals and hydrogen: facts, opportunities and challenges, *Angew. Chem. -Int. Ed.* (2023), e202301909, <https://doi.org/10.1002/anie.202301909>.
- [35] U. Nwosu, A. Wang, B. Palma, H. Zhao, M.A. Khan, M. Kibria, J. Hu, Selective biomass photoreforming for valuable chemicals and fuels: a critical review, *Renew. Sust. Energ. Rev.* 148 (2021), 111266, <https://doi.org/10.1016/j.rser.2021.111266>.
- [36] X. Wu, N. Luo, S. Xie, H. Zhang, Q. Zhang, F. Wang, Y. Wang, Photocatalytic transformations of lignocellulosic biomass into chemicals, *Chem. Soc. Rev.* 49 (2020) 6198–6223, <https://doi.org/10.1039/d0cs00314j>.
- [37] C. Zhou, J. Wu, Y. Li, H. Cao, Highly efficient UV-visible-infrared light-driven photothermocatalytic steam biomass reforming to H<sub>2</sub> on Ni nanoparticles loaded on mesoporous silica, *Energy Environ. Sci.* 15 (2022) 3041–3050, <https://doi.org/10.1039/d2ee00816e>.
- [38] H. Shi, C. Tian, X. Liu, N. Sun, C. Song, H. Zheng, K. Gao, X. Wang, Z. Jiang, Y. Xuan, Y. Ding, Ni-phyllosilicate nanotubes coated by CeO<sub>2</sub> for ultra-efficiency of 36.9% and near-limit CO<sub>2</sub> conversion in solar-driven conversion of CO<sub>2</sub>-to-fuel, *Chem. Eng. J.* 454 (2023), 140063, <https://doi.org/10.1016/j.cej.2022.140063>.
- [39] Q. Hu, Y. Li, J. Wu, Y. Hu, H. Cao, Y. Yang, Extraordinary catalytic performance of nickel half-metal clusters for light-driven dry reforming of methane, *Adv. Energy Mater.* 13 (2023), <https://doi.org/10.1002/aenm.202300071>.
- [40] L. Zhou, J.M.P. Martirez, J. Finzel, C. Zhang, D.F. Swearer, S. Tian, H. Robatjazi, M. Lou, L. Dong, L. Henderson, P. Christopher, E.A. Carter, P. Nordlander, N. Halas, Light-driven methane dry reforming with single atomic site antenna-reactor plasmonic photocatalysts, *Nat. Energy* 5 (2020) 61–70, <https://doi.org/10.1038/s41560-019-0517-9>.
- [41] G. Zhang, S. Wu, Y. Li, Q. Zhang, Significant improvement in activity, durability, and light-to-fuel efficiency of Ni nanoparticles by La<sub>2</sub>O<sub>3</sub> cluster modification for photothermocatalytic CO<sub>2</sub> reduction, *Appl. Catal. B-Environ.* 264 (2020), 118544, <https://doi.org/10.1016/j.apcatb.2019.118544>.
- [42] S. Wu, Y. Li, Q. Zhang, Q. Hu, J. Wu, C. Zhou, X. Zhao, Formation of NiCo alloy nanoparticles on Co doped Al<sub>2</sub>O<sub>3</sub> leads to high fuel production rate, large light-to-fuel efficiency, and excellent durability for photothermocatalytic CO<sub>2</sub> reduction, *Adv. Energy Mater.* 10 (2020), 2002602, <https://doi.org/10.1002/aenm.202002602>.
- [43] S. Wu, Y. Li, Q. Zhang, Z. Jiang, Y. Yang, J. Wu, X. Zhao, High light-to-fuel efficiency and CO<sub>2</sub> reduction rates achieved on a unique nanocomposite of Co/Co doped Al<sub>2</sub>O<sub>3</sub> nanosheets with UV-vis-IR irradiation, *Energy Environ. Sci.* 12 (2019) 2581–2590, <https://doi.org/10.1039/c9ee01484e>.
- [44] Q. Zhang, M. Mao, Y. Li, Y. Yang, H. Huang, Z. Jiang, Q. Hu, S. Wu, X. Zhao, Novel photoactivation promoted light-driven CO<sub>2</sub> reduction by CH<sub>4</sub> on Ni/CeO<sub>2</sub> nanocomposite with high light-to-fuel efficiency and enhanced stability, *Appl. Catal. B-Environ.* 239 (2018) 555–564, <https://doi.org/10.1016/j.apcatb.2018.08.052>.
- [45] H. Huang, M. Mao, Q. Zhang, Y. Li, J. Bai, Y. Yang, M. Zeng, X. Zhao, Solar-light-driven CO<sub>2</sub> reduction by CH<sub>4</sub> on silica-cluster-modified Ni nanocrystals with a high solar-to-fuel efficiency and excellent durability, *Adv. Energy Mater.* 8 (2018), 1702472, <https://doi.org/10.1002/aenm.201702472>.
- [46] M. Zhang, H. Gao, J. Chen, E.A. Elimian, H. Jia, Calcination engineering of urchin-like CoO<sub>x</sub>-CN catalysts to enhance photothermocatalytic oxidation of toluene via photo-/thermo- coupling effect, *Appl. Catal. B-Environ.* 307 (2022), 121208, <https://doi.org/10.1016/j.apcatb.2022.121208>.
- [47] H. Gao, X. Lv, M. Zhang, Q. Li, J. Chen, Z. Hu, H. Jia, Copper-cobalt strong interaction to improve photothermocatalytic performance of cobalt-copper oxides supported on copper foam for toluene oxidation, *Chem. Eng. J.* 434 (2022), 134618, <https://doi.org/10.1016/j.cej.2022.134618>.
- [48] E.A. Elimian, M. Zhang, J. Chen, H. Jia, Y. Sun, J. He, Construction of Pt-mTiO<sub>2</sub>/USY multifunctional catalyst enriched with oxygen vacancies for the enhanced light-driven photothermocatalytic degradation of toluene, *Appl. Catal. B-Environ.* 307 (2022), 121203, <https://doi.org/10.1016/j.apcatb.2022.121203>.
- [49] S. Ning, H. Ou, Y. Li, C. Lv, S. Wang, D. Wang, J. Ye, Co<sup>0</sup>-Co<sup>6+</sup> interface double-site-mediated C-C coupling for the photothermal conversion of CO<sub>2</sub> into light olefins, *Angew. Chem. -Int. Ed.* 62 (2023), e202302253, <https://doi.org/10.1002/anie.202302253>.
- [50] S. Ning, Y. Sun, S. Ouyang, Y. Qi, J. Ye, Solar light-induced injection of hot electrons and photocarriers for synergistically enhanced photothermocatalysis over Cu/Co/SrTiO<sub>3</sub> catalyst towards boosting CO hydrogenation into C<sub>2</sub>-C<sub>4</sub> hydrocarbons, *Appl. Catal. B-Environ.* 310 (2022), 121063, <https://doi.org/10.1016/j.apcatb.2022.121063>.
- [51] Q. Hao, Z. Li, Y. Shi, R. Li, Y. Li, S. Ouyang, H. Yuan, T. Zhang, Boron-doped CN supported metallic Co catalysts with interfacial electron transfer for enhanced photothermal CO hydrogenation, *Nano Energy* 102 (2022), 107723, <https://doi.org/10.1016/j.nanoen.2022.107723>.
- [52] J. Zhao, Y. Bai, X. Liang, T. Wang, C. Wang, Photothermal catalytic CO<sub>2</sub> hydrogenation over molybdenum carbides: crystal structure and photothermocatalytic synergistic effects, *J. CO<sub>2</sub> Util.* 49 (2021), 101562, <https://doi.org/10.1016/j.jcou.2021.101562>.
- [53] Y. Tong, L. Song, S. Ning, S. Ouyang, J. Ye, Photocarriers-enhanced photothermocatalysis of water-gas shift reaction under H<sub>2</sub>-rich and low-temperature condition over CeO<sub>2</sub>/Cu<sub>1-x</sub>Mn<sub>1-x</sub>O<sub>4</sub> catalyst, *Appl. Catal. B-Environ.* 298 (2021), 120551, <https://doi.org/10.1016/j.apcatb.2021.120551>.
- [54] L. Zhao, Y. Qi, L. Song, S. Ning, S. Ouyang, H. Xu, J. Ye, Solar-driven water-gas shift reaction over CuO<sub>x</sub>/Al<sub>2</sub>O<sub>3</sub> with 1.1% of light-to-energy storage, *Angew. Chem. Int. Ed.* 58 (2019) 7708–7712, <https://doi.org/10.1002/anie.201902324>.